Graphical Abstract

Correlation of 2D and 3D Particle Properties with Simulated Particle Imaging Dataset

Thomas Buchwald, Ralf Ditscherlein, Urs A. Peuker

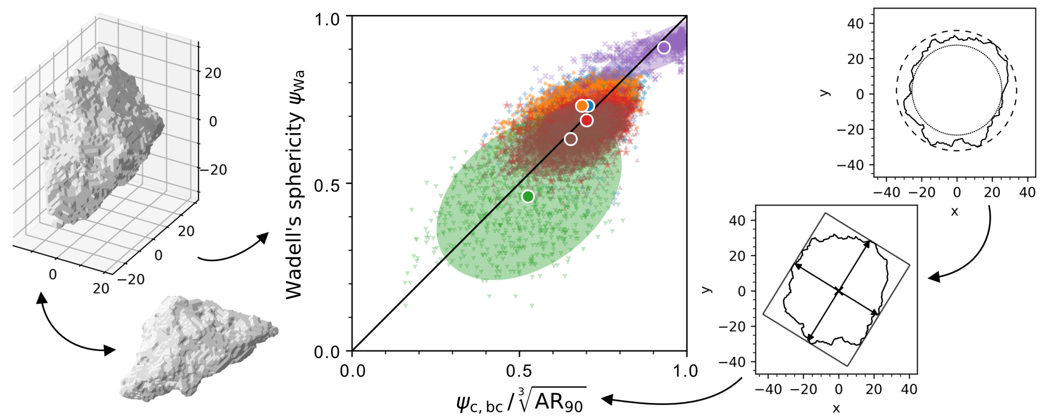

Highlights

Correlation of 2D and 3D Particle Properties with Simulated Particle Imaging Dataset

Thomas Buchwald, Ralf Ditscherlein, Urs A. Peuker

- Workflow for simulation of static and dynamic image analysis is presented.
- Particle characteristics for several solids types are determined.
- Influence of image analysis methods on shape factors are shown.
- A correlation for 3D sphericity from 2D shape factors is found.
- A correlation of particle width from 2D measures is found.

Correlation of 2D and 3D Particle Properties with Simulated Particle Imaging Dataset

Thomas Buchwald, Ralf Ditscherlein, Urs A. Peuker

Institute of Mechanical Process Engineering and Mineral Processing, TU Bergakademie Freiberg, Agricolastr. 1, 09599, Freiberg, Germany

Abstract

Particle size and shape characteristics are commonly measured with two-dimensional (2D) imaging techniques, two of which are static or dynamic imaging techniques. These 2D particle characteristics need to be applied to particulate processes where they model three-dimensional (3D) processes. The correlation between 2D and 3D particle characteristics is therefore necessary, but the knowledge is still limited to either mathematically simple shapes or specific sets of investigated bulk solids.

A particle dataset consisting of six bulk solids measured with X-ray microscopy was used to simulate the results of 2D imaging techniques to create a database to test the correlation between sets of particle characteristics. The dataset thus created offers the possibility to study the correlation between characteristic values and robustly predict the 3D properties of bulk solids measured with 2D measurement techniques. Several correlations are determined, including 2D shape factors vs. Wadell's sphericity (3D), and Feret diameters (2D) vs. particle width (3D).

Keywords: imaging techniques, static image analysis, dynamic image analysis, circularity, sphericity, shape factors, equivalent particle size, particle characteristics, correlation

1. Introduction

The characterization of particles regarding size and shape is essential for most particulate processes. Advances in measuring techniques have made the CT measurement of bulk solids and resulting particle-discrete datasets possible, enabling new methods of analyzing, e.g., separation processes [1, 2].

However, tomographic measurement is a time-consuming and costly process, so the characterization of bulk solids in everyday industrial and laboratory applications is mostly done with other well-established techniques. For the measurement of particle size and shape in orders of magnitude from 1 µm to 10 mm, static and dynamic image analysis are widely used, and have often replaced traditional sieve analysis [3, 4, 5]. Furthermore, inline particle measurements are becoming more abundant in research and industry [6, 7].

Wadell introduced the concept of sphericity to account for a particle sedimentation velocity deviating from the sedimentation velocity of a sphere [8, 9]. Sphericity has since been used by many researchers and practitioners to represent particle shape in a single value. But Wadell recognized that the true sphericity for single particles might be hard to come by – it was even deemed unmeasurable by peers [10] – so he proposed the measurement of the projection of a particle at rest and an alternative definition for sphericity from it (Eq. 14).

The classical approach by Zingg to classify particles into shape categories by the ratios of their principal dimensions (elongation and flatness) is still widely in use and has been recently implemented in a particle shape analysis tool [11, 12]. 2D aspect ratios, along with circularity and convexity, are recognized in the literature as meaningful shape descriptors [13].

Since Wadell, many people have investigated how 2D imaging techniques may accurately describe the "true", 3D particle shape [14, 15, 16, 17, 18, 19]. In many ways, this study tries to retrace the steps of Bagheri et al. [20], who compared computed tomography measurements with projection images to find correlations to accurately describe 3D shape. Whereas before a particle's three principal dimensions (length, width, and thickness) were defined as perpendicular to each other, with length being the dimension between the two points on the particle furthest from each other, the authors propose the determination from the two projections with minimum (for thickness) and maximum areas (for width and thickness). Their results are interesting, while lacking statistical robustness because of the small sample size.

To try to overcome the time-consuming task of measuring particles with computed tomography, several researchers have shown how to simulate realistic 3D particle data. Their work utilizes random fields [21] and spherical harmonics [22]. Additional work has been done on reconstructing 3D particles from 2D projections using convolutional neural networks [23, 24]. This happens in recognition of the approach of capturing single particles from multiple angles to describe the 3D particle shape [25, 26]. The other approach is to quantify particle shape accurately only in the statistical sense by measuring enough particles to have a good estimate of the mean particle shape of a given bulk solid [13].

In this study, we take the second approach by asking how well 2D descriptors can describe 3D particle shape. The text comprises two distinct parts. The first part is concerned with an expansive dataset of 3D particles provided by the PARROT particle database[1] [27] and the simulation of both static and dynamic image analysis. The resulting dataset is publicly available (see Supplementary Data) and it is our hope that it can serve as a foundation for investigation of many effects that accompany image analysis and that have yet to be properly quantified. The second part tries to correlate some 3D properties with 2D properties determined from the simulated particle projections. This part of the study, sections 4.1 through 4.2, is meant to prove how meaningful the developed dataset is.

2. Materials and Methods

2.1. Particle Characteristics

The term *particle characteristic* as used in this text includes all parameters that can describe the size and shape of a particle. It comprises three subgroups: *geometric properties*, *equivalent diameters* and *shape factors*. Geometric properties can be directly measured from the 2D or 3D representation of a given particle. Equivalent diameters are typically diameters of the circle (2D) or sphere (3D) that share one of the geometrical properties of the particle. Finally, shape factors are mostly ratios of two different geometrical properties, one of which may be calculated from the particle's convex hull.

[1]parrot.tu-freiberg.de

2.1.1. 2D Measures

These geometric properties can all be derived directly from the projection or section of a particle in any direction (Fig. 1b); therefore, they are applicable to all 2D imaging techniques, like static and dynamic image analysis.

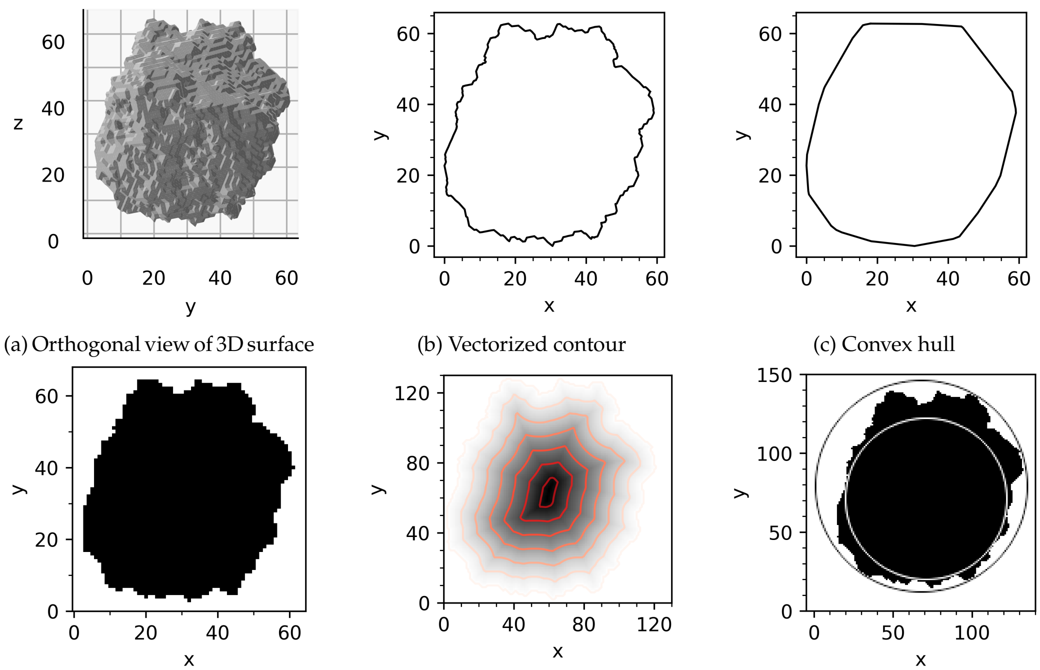

(a) Orthogonal view of 3D surface
(b) Vectorized contour
(c) Convex hull
(d) Pixelized projection
(e) Euclidian distance map with contours of same distance from projection border
(f) Minimum enclosing circle (black) and maximum inscribed circle (white)

Figure 1: Illustration of methods for generation of 2D descriptors for particle shape

In the current study, only the vector representation of the silhouette image is used. The accuracy of the calculated parameters therefore only depends on the resolution of the original 3D surface mesh and the marching cubes procedure [28] with which it was produced from the voxel representations that themselves originated in the reconstructed tomography image stack. The contour is voxelized solely to simplify the calculation of bounding circles, enabling the use of standard Python libraries. Both pixelization and orthogonal projection images, as shown in Fig. 1a, offer possibilities for testing the effects of image resolution and roughness measurement, respectively.

Area and perimeter. Both the projection area A_p and the perimeter P_p are calculated by methods provided by the `Shapely` package, directly from the projection contour, as shown in Fig. 1b. Because of the inherent fractal behavior of many real solids' surfaces, the perimeter is much less robust than the projection area for smaller particles. Still, the effect of measurement resolution will be more pronounced in the determination of the (3D) surface area, where surface roughness comes more into effect than in the 2D case [29].

Convex Hull. The convex hull is determined using a method of the `Shapely` polygon object that contains the contour. For the convex hull, both area A_c and perimeter P_c are determined.

Feret Diameters. Minimum and maximum Feret diameters are determined by brute force: the projection contour is rotated in 500 steps between 0° and 180°, and the boundaries in both axis directions are determined. The smallest measured distance between boundaries will be the minimum Feret diameter $x_\mathrm{Fe,min}$, while the largest distance will be the maximum Feret diameter $x_\mathrm{Fe,max}$. The two measures, $x_\mathrm{Fe,min}$ and $x_\mathrm{Fe,max}$, are shown in Fig. 2a. As can be seen, the two Feret diameters are not necessarily at a right angle, which is why two *additional* Feret diameters are determined: $x_\mathrm{Fe,min90}$ and $x_\mathrm{Fe,max90}$, which are perpendicular to the $x_\mathrm{Fe,max}$ and $x_\mathrm{Fe,min}$, respectively.

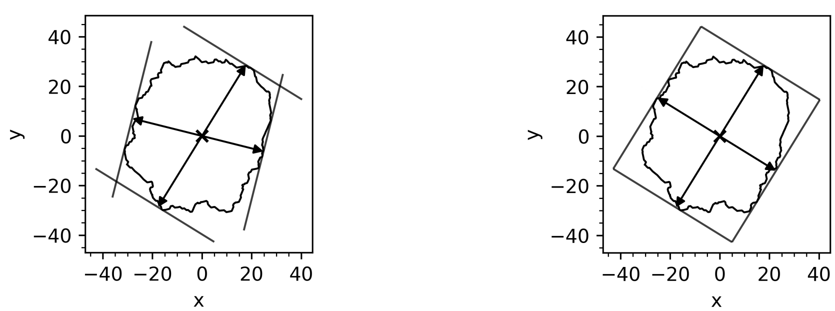

(a) Maximum $x_\mathrm{Fe,max}$ and minimum $x_\mathrm{Fe,min}$ Feret diameters

(b) Maximum $x_\mathrm{Fe,max}$ and perpendicular $x_\mathrm{Fe,min90}$ Feret diameters

Figure 2: Illustration of different definitions of Feret diameters

The use of perpendicular Feret diameters serves two purposes. Firstly, for static image analysis, the maximum and minimum Feret diameters will be very close to the length and width of a particle, respectively (Fig. 2b). Secondly, the (true) minimum Feret diameter $x_{\mathrm{Fe,min}}$ and its perpendicular Feret diameter $x_{\mathrm{Fe,max90}}$ will, in most cases, be very close to the actual dimensions of the oriented bounding box, i.e., the bounding box of least area.

Minimum Enclosing Circle. The diameter of the minimum enclosing circle d_{ec} belongs to the circle that has the least area while still containing the entire projection contour (Fig. 1f). While dedicated Python packages for the task of determining this measure exist, such as `miniball`, here, the computer vision library OpenCV was used [30].

For the calculation of d_{ec}, the contour needs to be transformed into an array first, equivalent to a pixel representation (Fig. 1d). The pixelization is achieved with the Python library `scikit-image`, which contains the `polygon` method that generates pixel coordinates inside a given polygon.

To increase the accuracy of d_{ec} (and d_{ic}), the contour coordinates are scaled up by a factor of 2 before pixelization, significantly affecting the results of both the center coordinate of the circle as well as its radius. Further scale-up is not considered necessary, or even useful, because the original 3D mesh does not offer more resolution anyway.

Maximum Inscribed Circle. The determination of the maximum inscribed circle d_{ic} for a 2D contour, as well as the maximum inscribed circle for a 3D surface, is not straightforward. For the authors, none of the methods found in literature were computationally efficient and more robust than a simple brute-force bisection algorithm.

A solution to efficiently determine the maximum inscribed circle was found by discretization of the contour, i.e., pixelization. The method uses the Euclidean distance transform as implemented in the Python library `scipy` [31]. The transform calculates the distance of each object pixel from the background (Fig. 1e). The pixel that contains the highest value after the transform will be the center of the maximum inscribed circle, while the corresponding pixel value will be $d_{\mathrm{ic}}/2$, i.e., the radius of the circle. The Euclidean distance transform is computationally inexpensive and is a relatively simple method for determining the maximum inscribed circle, as it transforms the problem from vector space to pixel space. This reduces the complexity of the problem significantly, albeit at the cost of being only as accurate as the pixel dimensions allow.

It has since been found that the method described here has been used in other particle-related research [32, 33].

2.1.2. 3D Measures

Volume and Surface Area. Both volume and surface area are properties of the `trimesh` object that contains the particle mesh, so it is defined by functions already implemented by the package.

However, using the surface area of the computed mesh leads to an error in the determination of Wadell's sphericity (cf. Eq. 8), where a maximum value of $\psi_{\mathrm{Wa}} \approx 0.92$ is reached even for highly spherical particles like soda-lime glass. This maximum sphericity value of $\psi_{\mathrm{Wa}} \approx 0.92$ stems from the conversion of the particle volumes from voxel representation to a triangular surface. The marching cubes algorithm interpolates between the edges of the voxels to smooth the surface, depending on the number and configuration of adjacent solid voxels [34, 35]. The resulting error will be 8 % to 9 % [36]. In comparison, the error in sphericity determination from the voxel representation for a sphere would be > 30 %, because of the greatly exaggerated surface area.

An alternative determination of surface area is achieved with the collection of plugins `MorphoLibJ` for ImageJ [37]. From it, the `ParticleAnalysis3D` plugin is used which computes the surface area of a 3D object with an N-dimensional extension of the Crofton formula [38, 39]. Note that the original Java libraries were used, accessed directly in Python through `Pyjnius`. The accuracy of the method was tested by producing incrementally larger spheres in discrete voxel representations and meshing them, using both voxel representation and mesh for the calculation of surface area and particle volume. The result is shown in Fig. 3, where Wadell's sphericity has been calculated using all three permutations of equivalent diameters calculated from two volume (x_{V}, Eq. 2) and two surface area (x_{S}, Eq. 3) definitions: $x_{\mathrm{V,voxel}}$ uses the volume equal to the number of voxels, $x_{\mathrm{V,mesh}}$ the volume contained in the mesh produced by the marching cubes algorithm, $x_{\mathrm{S,crofton}}$ the approximation of surface area with the 3D Crofton formula, and $x_{\mathrm{S,mesh}}$ the surface area of the mesh directly.

It can be seen that using volume and surface area of the mesh leads to a final sphericity value $\psi_{\mathrm{Wa}} < 1$, even for spheres of diameters larger than a hundred voxels. Using the information of the voxel representation directly, as used in `MorphoLibJ` will result in sphericity values $\psi_{\mathrm{Wa}} > 1$ for smaller spheres, which is also counterintuitive. The underlying problem

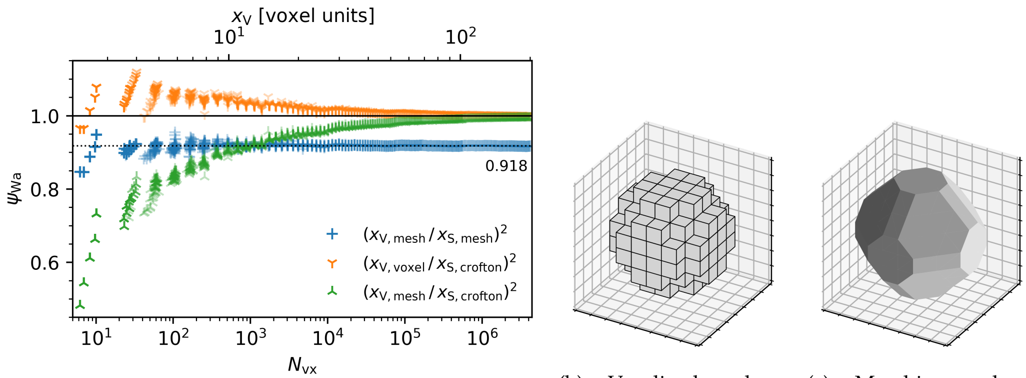

(a) Calculated sphericity values over number of voxels of sphere N_{vx} and volume-equivalent diameter x_V

(b) Voxelized sphere with a diameter of six voxels

(c) Marching cubes–meshed surface of the voxel object in Fig. 3b

Figure 3: Sphericity values for different definitions of particle surface area and volume, illustration of marching cubes meshing result

is that not every voxel must be fully filled by the particle and the volume approximated by counting the voxels is therefore too high. If the volume of the mesh is used instead of the volume of the voxelized particle, i.e., $x_{V,mesh}$ instead of $x_{V,voxel}$, the resulting sphericity values will approach the limit of $\psi_{Wa} \rightarrow 1$, with small spheres observing sphericity values $\psi_{Wa} < 1$. As this definition of sphericity, as shown by the green points in Fig. 3a, is the most intuitive and realistic one, the following strategy for 3D particle property determination is recommended and used in this study:

- particle volume V_p is determined directly from the particle mesh,
- particle surface area S_p is determined with the 3D Crofton formula as implemented in `MorphoLibJ`. For this, the particle mesh is voxelized again.

Specific Surface Area. A combination of volume and area, specific surface area is an important measure for all sorts of processes involving heat, moment, or mass transfer. It is defined as:

$$S_V = \frac{S_p}{V_p} \tag{1}$$

In contrast to most other particle properties, specific surface area will decrease with increasing particle volume. As explained above, the surface area S_p is calculated from the voxelized surface, while the particle volume V_p is computed from the meshed surface.

Convex Hull. The convex hull is another property of the `trimesh` object, from which both volume V_c and surface area S_c can be calculated.

Aligned Bounding Box. In this study, a bounding box defines the main dimensions of the particle. The aligned bounding box defines the length l, width w, and thickness t to be the longest, intermediate, and shortest edge lengths. This approach is congruent with the definition of particle dimensions by Krumbein, who measured orthogonal lengths starting with the longest one found on the particle [40], which is equivalent to the maximum Feret diameter.

The aligned bounding box is created by tranformation of the particle so that its principal axes of inertia align with the cartesian dimension vectors (Fig. 4b). The necessary transform is again a property of the `trimesh` object containing the particle mesh. After the transformation, the bounding box, again, is a property of the `trimesh` object (Fig. 4d).

The definition of 3D particle dimensions in this way also makes it possible to directly compare measurements with static image analysis simulation results. When the maximum Feret $x_\mathrm{Fe,max}$ and the perpendicular Feret diameter $x_\mathrm{Fe,min90}$ (Fig. 2b) are used, they will be identical with length l and width w for the aligned particle (section 3.1). For stable positions, section 3.2, $x_\mathrm{Fe,max}$ should still reflect actual particle length l, while $x_\mathrm{Fe,min90}$ should differ somewhat because the true particle width is oriented at an angle to the projection direction, i.e., surface normal.

Bagheri et al. favoured the use of uncorrelated Feret extrema for the determination of particle dimensions to reduce operator error [20]. However, with most modern measurement setups particle dimensions are seldom determined manually, and determination of a minimum Feret diameter for compact projections may still be difficult if done manually anyway.

Oriented Bounding Box. The oriented bounding box is again calculated by `trimesh` for a given particle mesh and represents the bounding box of least volume that still contains the whole mesh surface (Fig. 4c). The dimensions of the oriented bounding box are determined from the Cartesian coordinates after applying the inverse transform on the bounding box, since the oriented bounding box is likely to be at random angles toward the Cartesian axes, even if the particle was first aligned to its principal axes of intertia.

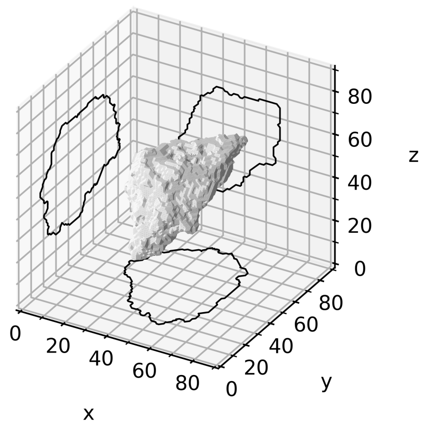

(a) 3D particle in its original position

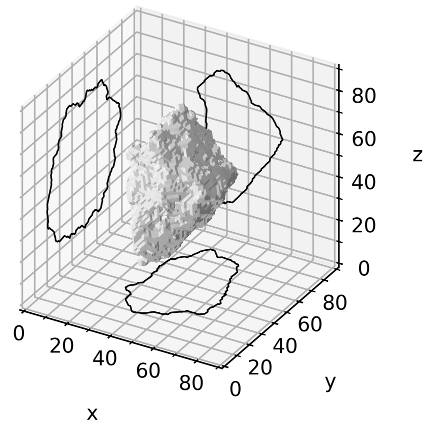

(b) 3D particle of 4a after applying the principal axis alignment transform

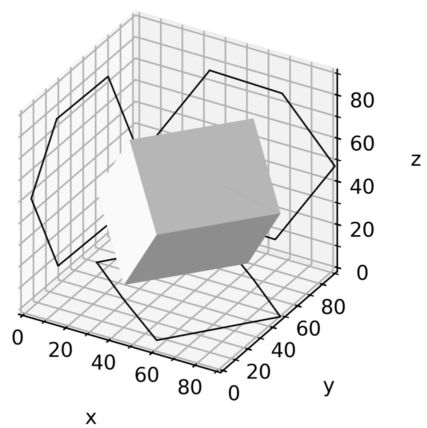

(c) Oriented bounding box for particle in 4a, $V = 121\,486$

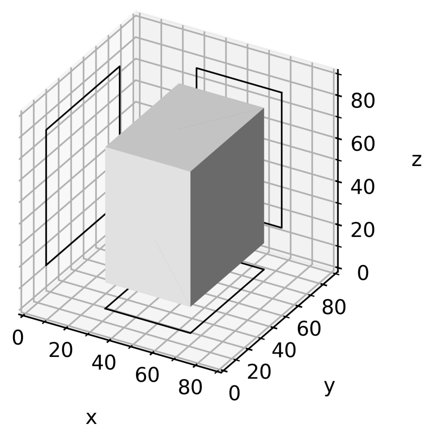

(d) Bounding box along Cartesian axes for aligned particle in 4b, $V = 146\,740$

Figure 4: Illustration of the two different definitions for bounding boxes, volumes given in axis units

Fig. 5 shows comparisons of the dimensions of aligned bounding boxes and oriented bounding boxes for all investigated particles. The oriented bounding box has on average smaller dimensions than the aligned bounding box. The effect increases for the longer dimensions: length will mostly be smaller for the oriented bounding box, whereas there is a more random scatter for thickness.

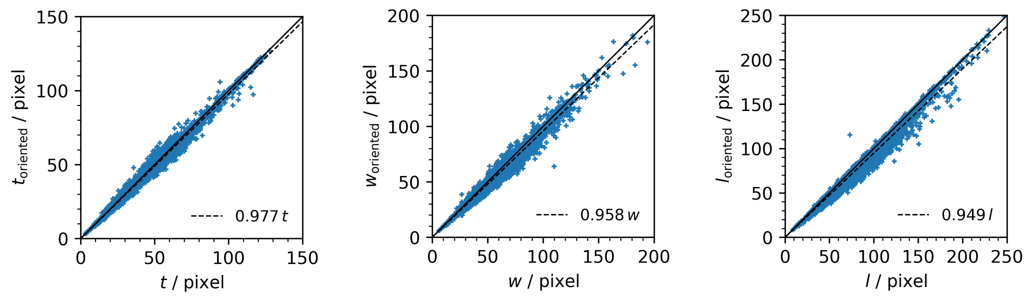

(a) Thickness (b) Width (c) Length

Figure 5: Comparison of dimensions determined by aligned and oriented bounding boxes

On average, the oriented bounding box will be 14 % smaller than the aligned bounding box for compact particles. In contrast, the oriented bounding box will only be 12 % smaller for mica particles which, because of their flat nature, should, in their aligned position, already be closer to the smallest box possible. Finally, soda-lime glass spheres have on average oriented bounding boxes that are only 5.5 % smaller.

The aligned bounding box is preferred here over the oriented bounding box because of its congruence with Krumbein's definition who chose it because it is easier to understand and determine by the practitioner.

Bounding Spheres. The minimum bounding sphere again is a property of the mesh object defined by the `trimesh` library, so the diameter of the minimum enclosing sphere d_{es} is determined in a single line of code. A visualization of both bounding spheres is found in Fig. 6.

The maximum inscribed sphere is approximated as the maximum inscribed circle in the 2D case. In both cases, the function `distance_transform_edt` from the `scripy` library [31] is used to calculate the Euclidean distance transform to find the pixel/voxel that is furthest from the particle surface. This maximum value will be the diameter of the maximum inscribed sphere d_{is}.

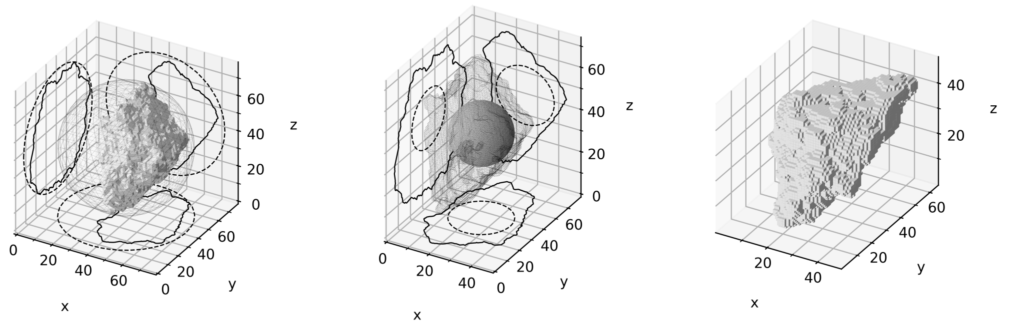

(a) Minimum enclosing sphere (b) Minimum inscribed sphere (c) Voxelized particle from original surface in Fig. 4a

Figure 6: Illustration of both minimum enclosing sphere and maximum inscribed sphere

In order to perform the Euclidean distance transform, the surface mesh needs to be discretized into a voxel representation (Fig. 6c). The voxelization is also done with methods provided by `trimesh`, and, as with the 2D case, at a scale factor of 2, which increases the accuracy of the diameter estimation significantly. Care must be taken to produce a filled voxel representation: most voxelization algorithms will only return solid voxels where the surface of the mesh touches. An extra step is involved to fill the hollow discretized surface with `scipy`'s method `binary_fill_holes`.

2.1.3. *Equivalent Diameters*

Several properties in 2D and 3D can be compared to that of the idealized shapes, a circle in two and a sphere in three dimensions. In 3D, the diameter of a sphere can be calculated that has the same volume V_p as that of the particle. This diameter will be called the volume-equivalent diameter:

$$x_\mathrm{V} = \sqrt[3]{\frac{6V_\mathrm{p}}{\pi}} \tag{2}$$

In the same sense, the diameter of the sphere that has the same surface area S_p as that of the particle (surface-equivalent diameter) is:

$$x_\mathrm{S} = \sqrt{\frac{S_\mathrm{p}}{\pi}} \tag{3}$$

In two dimensions, the particle properties volume V_p and surface area S_p reduce to projection properties, projection area A_p and perimeter P_p.

The diameter of the circle that has the same area as the projection area, the area-equivalent diameter, is:

$$x_{\mathrm{A}} = \sqrt{\frac{4A_{\mathrm{p}}}{\pi}} \tag{4}$$

Lastly, the perimeter-equivalent diameter is the diameter of the circle that has the same perimeter as that of the particle projection, defined as:

$$x_{\mathrm{P}} = \frac{P_{\mathrm{p}}}{\pi} \tag{5}$$

2.1.4. Shape Factors

Shape factors are derived from two or three of the particle properties or equivalent diameters introduced above. All shape factors described below are dimensionless, which means they can be used to good effect to find correlations between 2D projections and 3D particle properties.

Length Ratios. Flatness t/w and elongation w/l have been used before in Fig. 8d to classify particles into shape categories.

In 2D, two more length ratios are used in this study. First the aspect ratio is defined as the ratio of minimum and maximum Feret diameter:

$$\mathrm{AR} = \frac{x_{\mathrm{Fe,min}}}{x_{\mathrm{Fe,max}}} \tag{6}$$

As discussed before, the two Feret diameters often at an angle $\neq 90°$. Because the 3D particle dimensions are defined by their bounding boxes, they are necessarily at a right angle to each other. It therefore makes sense to define an additional, orthogonal aspect ratio of perpendicular Feret diameters:

$$\mathrm{AR}_{90} = \frac{x_{\mathrm{Fe,min90}}}{x_{\mathrm{Fe,max}}} \tag{7}$$

Sphericity. Several shericity definitions exist, some of them fundamentally different from each other, but for all of them, the sphericity $\psi < 1$ for particles deviating from a sphere.

The original definition of sphericity comes from Wadell for application on sedimentary particles [8]. Wadell defined sphericity as the ratio of the surface area of a sphere of equal volume as that of the particle to the actual surface area of the particle:

$$\psi_{\mathrm{Wa}} = \frac{S_{\mathrm{sp}}}{S_{\mathrm{p}}} = \left(\frac{x_{\mathrm{V}}}{x_{\mathrm{S}}}\right)^2 \tag{8}$$

S_{sp} is the surface area of the sphere having the same volume as the particle.

Krumbein defined a sphericity by comparing a given particle to a triaxial ellipsoid [40]. After determining the longest dimension of the particle, the second longest dimension *perpendicular* to the first is determined, with the third dimension being perpendicular to the other two. In this sense, the three dimensions are equivalent to length l, width w, and thickness t of the bounding box of the principally aligned particle, as described in section 2.1.2.

$$\psi_{\mathrm{Kr}} = \sqrt[3]{\frac{w\,t}{l^2}} \tag{9}$$

Another definition for sphericity has been defined by Sneed and Folk as $\psi_{\mathrm{SF}} = \sqrt[3]{t^2/(w\,l)}$ [41], but will not be used in this study.

Another sphericity definition is the ratio of the diameters of the two bounding spheres, i.e., maximum inscribed sphere to minimum enclosing sphere [42]:

$$\psi_{\mathrm{bs}} = \frac{d_{\mathrm{is}}}{d_{\mathrm{es}}} \tag{10}$$

Lastly, Hofmann applied the concept of statistical entropy to the particle shape description [43]:

$$\psi_{\mathrm{Ho}} = \frac{1}{\ln(1/3)} \sum_{i=1}^{3} p_i \ln p_i \ , \tag{11}$$

where $p_i = \frac{d_i}{d_1+d_2+d_3}$, $d_1 = l$, $d_2 = w$, and $d_3 = t$.

Hofmann's sphericity is supposed to be the most representative measure for the prediction of particle settling velocity [44].

Circularity. "Circularity" is the name chosen according to the definitions of Wadell [9] for the 2D equivalent of sphericity, basically a "projection sphericity", sometimes also called "roundness" [45]. Like sphericity, circularity approaches a value of one for particles that closely resemble circular shapes and will decrease in value for particles becoming less compact.

The original circularity definition as ratio of perimeter of the area-equivalent circle to the actual projection perimeter is due to Wadell [9]. Wadell stressed that circularity and sphericity are fundamentally different from roundness in the sense that roundness is a mesoscopic measure and circularity is a macroscopic measure. In other words, circularity and sphericity show *shape* deviations, whereas roundness shows *surface* deviations.

$$\psi_{\mathrm{c}} = \frac{P_{\mathrm{c}}}{P_{\mathrm{p}}} = \frac{x_{\mathrm{A}}}{x_{\mathrm{P}}} = \sqrt{\frac{4\pi A_{\mathrm{p}}}{P_{\mathrm{p}}^2}} \tag{12}$$

The square of circularity ψ_{c} is called the form factor and is equivalent to the "roundness" factor defined by Cox [46, 47, 48].

$$\mathrm{FF} = \frac{4\pi A_{\mathrm{p}}}{P_{\mathrm{p}}^2} \tag{13}$$

Because one early criticism of ψ_{Wa} was the difficulty of measurement, Wadell proposed more easily attainable circularity measure:

$$\psi_{\mathrm{c,Wa}} = \frac{x_{\mathrm{A,stable}}}{d_{\mathrm{ec}}} \tag{14}$$

In the above equation, $x_{\mathrm{A,stable}}$ is the diameter of a circle of equal projection area as that of a given particle *at rest*, i.e., lying on a surface in a stable position. d_{ec} is, as per previous definition, the diameter of the minimum enclosing circle.

Another method of defining circularity is through both bounding circles, i.e., the radius of the maximum inscribed circle d_{ic} and the radius of the minimum enclosing circle d_{ec}:

$$\psi_{\mathrm{c,bc}} = \frac{d_{\mathrm{ic}}}{d_{\mathrm{ec}}} \tag{15}$$

Eq. 15 is the square of the circularity definition by Riley [45].

Solidity. As a measure of concavity, a solidity factor S_x can be calculated in both 2D and 3D. It compares the actual particle volume or projection area to its convex hulls. If there are no concavities, the solidity will be 1 and the particle or projection will be its own convex hull.

$$S_{x,3D} = \frac{V_p}{V_c} \tag{16}$$

$$S_{x,2D} = \frac{A_p}{A_c} \tag{17}$$

Convexity. Another measure for deviation from a convex object is the convexity, for which the symbol C_x is used. It compares the surface of particle or projection directly to the convex hull.

$$C_{x,3D} = \frac{S_c}{S_p} \tag{18}$$

$$C_{x,2D} = \frac{P_c}{P_p} \tag{19}$$

2.2. Particle Datasets

2.2.1. Acquisition

The solids particle data used in this study was prepared previously for the stated purpose of providing reference 3D datasets. A methodology was developed to produce isolated, i.e., non-touching, particles in a wax matrix [49, 50]. Tomographic reconstruction of X-ray microscopy measurements of these wax matrices offers the possibility to easily segment and extract the single 3D particles. The particle data is available in the form of the original reconstructed tomography stacks as well as single particle surfaces in STL format in the dedicated particle database PARROT [27].

VTK files that represent cropped voxel-based regions of interest for every particle from the tomographic reconstructions were used to recalculate STL meshes for the particles, as some STL surfaces in the PARROT dataset were not watertight, which would have led to problems in later analysis. The STL data used in this study is available in the supplementary data.

Table 1 gives an overview of the six solids of which particle surface data has been used. The particle size distributions are shown in the form of cumulative sums in Fig. 7. Thee solids are typically in a particle size range between 50 µm to 300 µm. The X-ray microscopy measurements were performed for a final voxel size, i.e., edge length, of 2 µm.

Table 1: Used particle systems, provided in the PARROT particle database [27]

type	production process	particle size	particles
aluminium oxide	crushing	55 µm to 200 µm	1571
dolomite	calcination and crushing	90 µm to 200 µm	642
soda-lime glass	spray drying	150 µm to 300 µm	602
limestone	dry milling	55 µm to 200 µm	1271
mica	comminution and magnetic separation	90 µm to 300 µm	415
quartz	crushing	$<$ 200 µm	1656

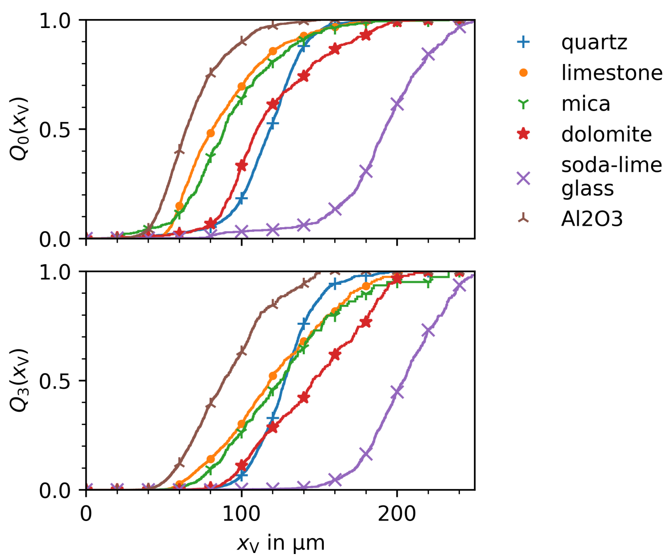

Figure 7: Number-base (Q_0) and volume-based (Q_3) particle size distributions for the six solids provided by the PARROT database

2.2.2. *Description*

The properties of the six solids (cf. Table 1) are shown in Fig. 8. From the plot of sphericity ψ_{Wa} over volume-equivalent diameter (Eqs.8 and 2) in Fig. 8a, it can be seen that four solids—quartz, limestone, dolomite, and aluminum oxide—are clustered in the same area with relatively high sphericity values of $\psi_{\mathrm{Wa}} > 0.5$. The soda-lime glass particles are the largest and also have the highest sphericity values. The high sphericity values can be traced to the production process by spray drying, resulting in mostly spherical shapes. In contrast, the mica particles show very low sphericities.

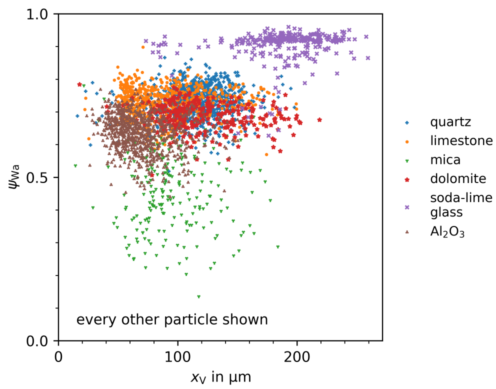

(a) Sphericity vs. particle size

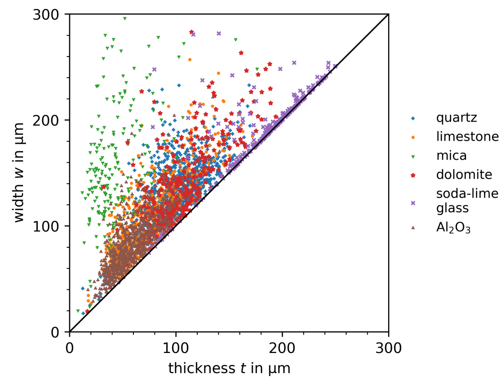

(b) Width vs. thickness

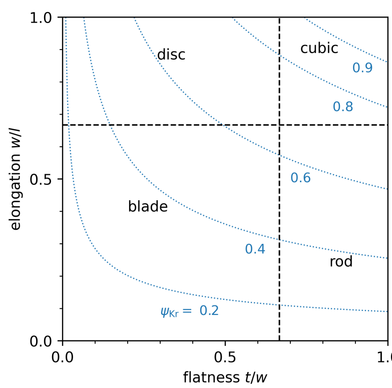

(c) Explanation of particle shape classification chart in Fig. 8d; isolines show values for Krumbein's sphericity ψ_{Kr}

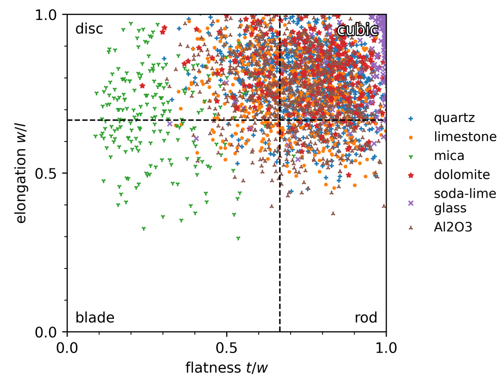

(d) Zingg's particle shape classification chart for aspect ratios of the three particle dimensions, elongation w/l and flatness t/w

Figure 8: Properties of the six particle datasets

In Fig. 8d, the particles are plotted along two aspect ratios, flatness t/w and elongation w/l, which makes classification according to particle shape possible. l, w, and t are the three main dimensions of a particle: length, width, and thickness, respectively, defined by the aligned bounding box (cf. section 2.1.2). The plot was first introduced by Zingg and later developed by Krumbein and Janoo [11, 40, 51]. Fig. 8c serves as an explanation, also showing isolines for sphericity, though Krumbein's sphericity definition is used, cf. Eq. 9. Alternative descriptors for the particle shape groups "disc," "cubic," and "rod" are "oblate," "compact," and "prolate," respectively [52].

Soda-lime glass spheres are expectedly clustered at values close to one for both aspect ratios, while the majority of particles of the other solids are mostly compact and could be classified as cubic and slightly rod- or disc-shaped, depending on their particular flatness or elongation values. In contrast, the mica particles are very flat and may be classified as disc- and blade-like.

Fig. 9 provides an example for each of the four categories according to the Zingg classification chart. The examples also serve to give an impression of what the different solids look like. While most of the limestone and quartz particles can be classified as compact/cubic, the two particles shown in Figs. 9a and 9d can be clearly identified as belonging to their respective categories of disc- and rod-like. The soda-lime glass particles are mostly near-perfect spheres, resulting in the aforementioned high sphericity values. The mica is mostly flaky in nature, resulting in very low flatness values, an effect that can be predicted from the plot of width vs. thickness in Fig. 8b.

Because their properties are very similar, the group of quartz, limestone, dolomite, and aluminum oxide will be grouped as "compact particles" in section 3.

2.3. 2D Imaging Simulation

2.3.1. Static Image Analysis

Static image analysis, as defined by ISO 13322-1, involves image acquisition to determine particle size where the particles are not moving against the axis of the optical equipment [53]. If a particle is large enough that adhesion forces with respect to the surface it is resting on are negligible, the particle will orient itself in a position in which at least its longest dimension is measurable. Two possibilities for the simulation of static image analysis were calculated:

- alignment of the principal inertia vectors on the Cartesian axes and
- alignment of the particle in one of its stable resting positions.

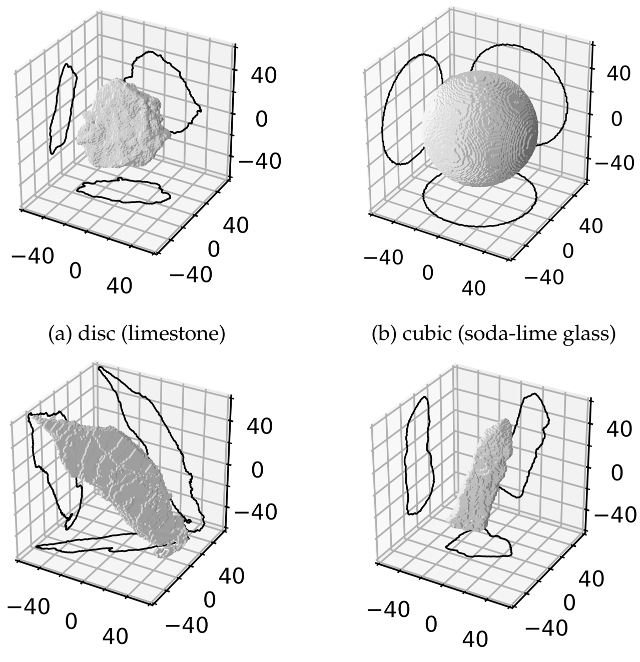

(a) disc (limestone) (b) cubic (soda-lime glass)

(c) blade (mica) (d) rod (quartz)

Figure 9: Examples from the datasets for particles belonging to the four shape categories of Figs. 8c and 8d with solid type in brackets

3D manipulation of the provided STL files was done with the Python library `trimesh`, which, as the name implies, focuses on triangular meshes [54]. The `trimesh` package offers options for both the procedures named, in particular a method that returns a list of the most likely stable positions of a given mesh, containing both the necessary transform and the respective probability of the particle settling in this position. Any resting positions with a probability $p > 0.1$ were used for further 2D analysis. Because highly spherical particles can easily have no positions of especially high resting probability, for each particle *at least* the two most probable positions were calculated. Fig. 10 gives an example of the stable positions of a particle and the resulting projections, in this case in z-direction, i.e., onto the xy-plane.

The imaging simulation involves getting the projection perpendicular to the plane that acts as the resting surface when calculating the stable position transforms (xy). For the mesh aligned along its principal inertia vectors, the projection is calculated perpendicular to the plane that contains the two major inertia vectors: when considering the aligned particle in Fig. 4b, the projection would be in direction of the x vector, onto the yz plane.

The subsequent procedure involves a custom function that calculates the orthogonal projection of the triangular mesh onto a plane defined by a given normal. With a given plane normal, the particle is first rotated to the correct position, and a projection transform is performed onto the yz (x-axis) plane (Fig. 1a). The projected triangles are then transformed into a single 2D polygon using the Python package Shapely [55]. Thus, a single contour is returned which can be used for further analysis. The relevant code can be found in the supplementary materials, see section 6.

In principle, the effects of image resolution may be investigated by scaling the projection and calculating a masked array that represents the pixel image. However, pixelization in this sense has only been used for the calculation of the enclosing and inscribed circles, cf. section 2.1.1.

2.3.2. Dynamic Image Analysis

In contrast to static analysis, dynamic image analysis is concerned with the image acquisition and analysis of moving particles [56]. Particles are therefore imaged in random orientations, unless the flow is highly turbulent. Depending on the setup, particles may be imaged more than once if they are not fast enough to leave the field of view. In many dynamic image analysis devices, these images will be taken as separate particle entities, while devices exist that track the particle while moving through the field of view to measure as many rotations as possible, e.g., the Camsizer 3D (Microtrac).

The procedure to produce a projection image is mostly the same as before, except that the particle is first rotated randomly. For every particle, three random orientations were used to produce projections, thereby increasing the number of simulated data points. Of course, the number of projections can be increased at will; however, to stay in line with the number of projections achieved through the stable positions as described in the previous section, three positions were considered sufficient. A larger dataset of ten projections per particle has been produced as well; however, the results achieved with it are the same as with the smaller one.

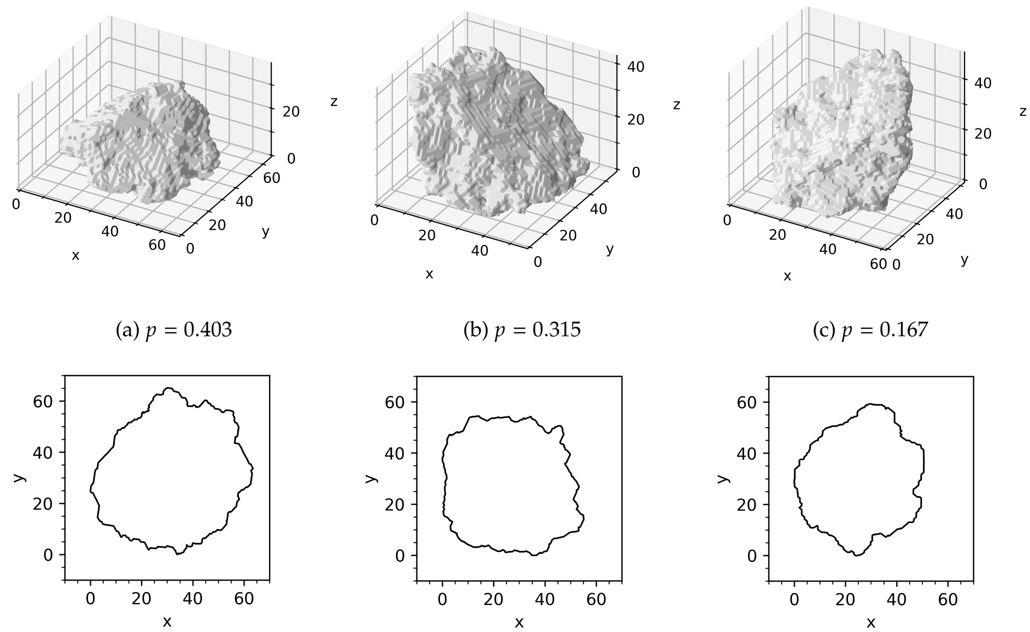

(a) $p = 0.403$ (b) $p = 0.315$ (c) $p = 0.167$

(d) (e) (f)

Figure 10: Stable position of the particle shown in Fig. 4 with the respective occurrence probabilities (Figs. 10a, 10b, and 10c) and resulting projection silhouettes along z-axis (Figs. 10d, 10e, and 10f)

3. Simulation Results

With the methods given above, a dataset was produced that contains the properties of the 3D particles and properties of their respective projections, produced in aligned, resting, and random orientations. The aligned orientations table naturally contains a single projection per particle, so 6157 in total. The stable orientations table contains, on average, three projections per particle for a total of 19 720 projections, though the absolute number per particle varies, cf. section 3.2. For random orientations, every particle produced three projections, for a total of 18 471.

3.1. Aligned Orientation

The aligned projection dataset is in many ways the simplest one and is used for verification of the analysis methods which are then used for the datasets of stable orientations and random projections. Because there is exactly one aligned projection for every particle, there are as many projections as particles in the complete dataset of all solids, 6157 in total. Because of the large number of particles, any effects found are considered at least *interesting*, though maybe not statistically robust.

Overall, 49 particle characteristics are calculated and used to build a correlation matrix, 25 comprising 3D and 24 comprising 2D measures and descriptors. Table B.1 lists all particle characteristics. The characteristics have been grouped into categories for easier comprehension of the correlation matrix.

A resulting matrix of Pearson correlation coefficients is shown in Fig. 11a. The resulting 49×49 grid contains many duplicates as well as areas not necessarily interesting, like the correlation of 2D and 3D parameters against themselves. The more interesting part of the matrix is the upper right or lower left quadrant, where the correlations between 2D and 3D characteristics are shown. This is why Fig. 11b only shows the upper right quadrant. From Arabic numbers and Roman numerals a specific characteristic may be determined with Table B.1.

Furthermore, only the compact particles (quartz, limestone, dolomite, and aluminium oxide) are used to calculate the correlation matrices. This is to avoid errors from the highly spherical soda-lime glass particles, as discussed in section 2.2.2, and the much higher scatter introduced by the plate-like mica.

Because some correlations are not linear, e.g., between equivalent diameters and specific surface area, the Spearman rank coefficient is chosen over the Pearson correlation coefficient. When comparing the two correlation matrices of Fig. 11, the choice of the Spearman rank coefficient (Fig. 11b) indeed results in much higher values. Values greater than zero will signify a positive correlation, whereas, if rarely, negative values will signify negative correlations.

The comparison of different geometric measures and/or equivalent diameters will result in very high correlations, as observed by the much more pronounced coloring of the upper left area of Fig. 11b. The brighter regions of less correlation are all in areas where shape factors are compared with geometric measures, equivalent diameters, or other shape factors. This behavior should be expected, because geometric properties all scale with absolute particle size, while shape factors are limited to the unit interval $[0, 1]$.

The most fruitful task is to search for high coefficient values where

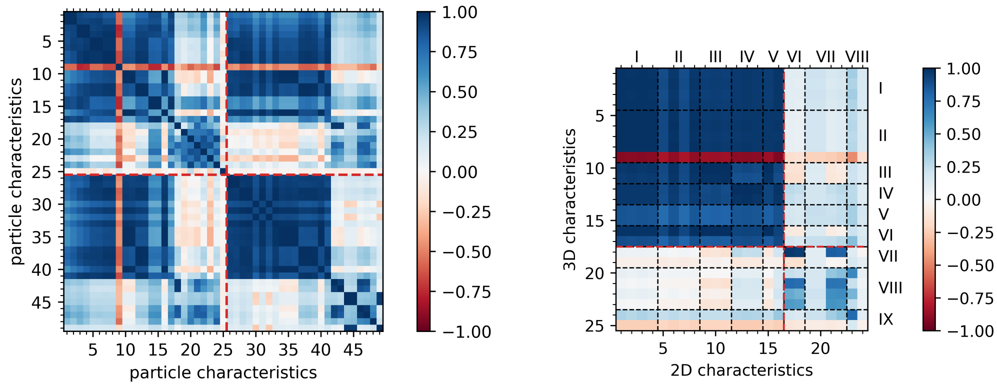

(a) Correlation matrix showing standard correlation coefficient between all computed particle characteristics *for all particles*; 3D characteristics before, 2D after the dashed red line

(b) Spearman rank correlation coefficient matrix *for compact particles* only

Figure 11: Correlation matrices for particle characteristics determined from *aligned projections*; Fig. 11b only shows the first quadrant (upper right) of the complete correlation matrix, with dashed red lines separating geometric properties and equivalent diameters from shape factors (cf. Table B.1 for a list of parameters)

2D and 3D shape factors are correlated, which is the lower right area of the correlation matrix in Fig. 11b. Because of the definition of particle dimensions via the bounding boxes, elongation w/l (18 in Fig. 11b) will correlate very well with aspect ratio AR (17), though the correlation with AR_{90} (18) naturally is perfect.

Interestingly, elongation (18) also correlates well with Wadell's alternative circularity definition $\psi_{\mathrm{c,Wa}}$ (21) and the bounding circles circularity ψ_{bc} (22). In a sense, ψ_{bc} forms a kind of aspect ratio, which is why it scales well with elongation: the inscribed d_{ic} and enclosed circle diameters d_{ec} show good correlation with minimum $x_{\mathrm{Fe,min}}$ and maximum Feret diameters $x_{\mathrm{Fe,max}}$, respectively. Krumbein sensibly took the square of elongation in his sphericity definition, Eq. 9, because elongation is a much better descriptor for the overall change from the cubic shape than flatness. In this sense, Krumbein's sphericity (21) shows pronounced, but not as high, correlations with the aspect ratios (17, 18) and Wadell's (21) and bounding circles circularity (22). The relationship between $\psi_{\mathrm{c,Wa}}$ and ψ_{bc} is briefly explored in Appendix A.

A final notable correlation is found between the 3D (24) and 2D solidities (23), indicating that 2D solidity is a good indicator of its 3D counterpart. However, the correlation is not linear and found to be $S_{\mathrm{x,3D}} \approx S^{n}_{\mathrm{x,2D}}$, with

$n = 3$ to 4.

3.2. *Stable Orientation*

As described in section 2.3.1, at least the two most probable resting positions were used to produce projections. However, it is instructive to plot the distribution of stable positions with a probability $p > 0.1$ per solids type, as shown in Fig. 12a.

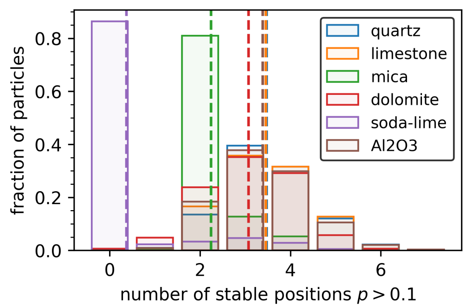

(a) Distribution of stable positions of all solids; dashed vertical lines indicate mean number of positions

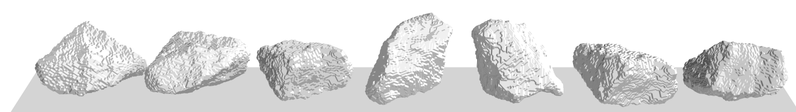

(b) Stable positions of a single limestone particle

Figure 12: Stable positions of investigated solid particles for a position probability of $p > 0.1$

Again, the soda-lime glass and mica particles clearly deviate from the compact particles (quartz, limestone, dolomite, and aluminium oxide). The compact particles on average have three to four stable positions. There are some outliers at six and even seven stable positions. One limestone particle is shown in its seven stable positions in Fig. 12b. In contrast, the soda-lime glass spheres have no stable positions $p > 0.1$ for 80 % of particles. The flaky mica particles expectedly find stable resting positions only on either of their flat sides, and so obtain on average two stable positions.

For the simulation of static image analysis via stable positioning, the correlation matrix in Fig. 13a exhibits a slight drop in very high correlations. The correlations found between shape factors for aligned projections (Fig. 11b) are still present though.

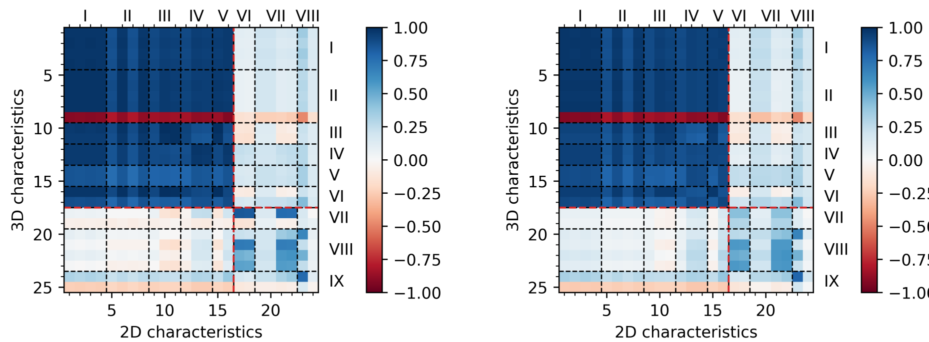

(a) Correlation matrix *stable positions*

(b) Correlation matrix for *random orientations*

Figure 13: Correlation matrices of Spearman rank correlation coefficients for *compact particles* and *random orientations*; dashed red lines separate geometric properties and equivalent diameters from shape factors (cf. Table B.1 for a list of parameters)

A typical example of decreasing correlation coefficients are the 3D particle widths (IV, 12/13) compared with minimum Ferets (12, 13) and 2D bounding box width (14). The reason is that a particle at an angle will not show its true width w anymore. Compared to the aligned projections, the correlation between elongation (18) and aspect ratios (VI, 17/18) is therefore slightly decreasing. Fig. 14 shows the correlation of several Feret diameters with their respective 3D particle dimensions. The perpendicular definition of minimum Feret $x_{\mathrm{Fe,min90}}$ scatters around the "true" particle width, whereas the true minimum Feret $x_{\mathrm{Fe,min}}$ systematically underestimates it. $x_{\mathrm{Fe,min90}}$ is therefore considered the more suitable estimate of particle width. Because of the definition of elongation w/l via the aligned bounding box, it will be better estimated by the orthogonal aspect ratio AR_{90} then the unaligned aspect ratio AR.

Of course, most correlations between 2D and 3D particle characteristics for static image analysis, as was discussed in this and the previous section, could have been found from careful thought experiments. Wadell based his alternative sphericity definition (Eq. 14) on a projection of a particle at rest exactly because length and width should always be measurable in this situation, and most shape factors should scale will with the derived aspect ratio/elongation, as long as the particles are not deviating too much from the cubic shape.

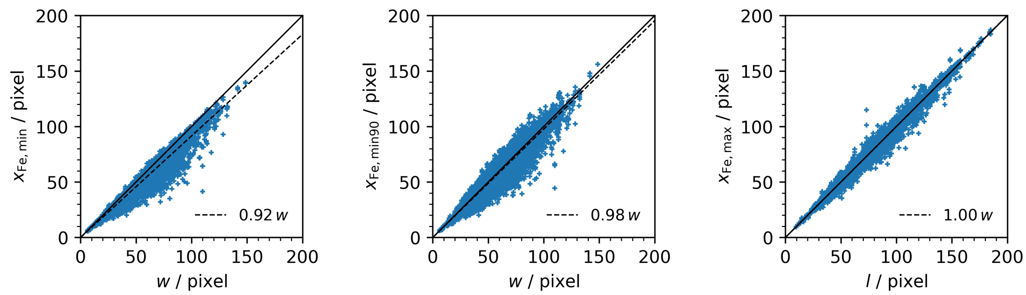

(a) Minimum Feret vs. width

(b) Orthogonal minimum Feret vs. width

(c) Maximum Feret vs. length

Figure 14: Comparison of Feret diameters to 3D measures *for all solids* in stable positions (static image analysis simulation)

3.3. Random Orientation

When comparing the correlation matrices of the stable position analysis (Fig. 13a) and that for dynamic simulation, i.e., projections of particles at random orientations (Fig. 13b), the amount of correlation is notably decreasing.

Mostly, the properties of the 3D convex hull, V_c (2), $x_{V,c}$ (4), S_c (6), $x_{S,c}$ (8), and S_V (9) scale well with projection area–related characteristics A_c (1), x_A (2), A_c (3), and $x_{A,c}$ (4). Additionally, the 3D convex hull's surface area (6, 8) correlates well with the 2D convex hull's perimeter (6, 8). However, remember that the Spearman rank correlation coefficient is used: correlations here need not be linear.

In case of the derived shape factors, the only good correlation exists between 3D (24) and 2D solidity (23), $S_{x,3D}$ and $S_{x,2D}$, respectively. Otherwise, correlation between shape factors has decreased considerably.

In the following, relationships between 2D and 3D particle properties are investigated more closely. These investigations serve as examples on how the described dataset may be used for further insights by interested researchers.

4. Correlations

4.1. Cauchy's surface area formula

The relationship between projection area and particle surface area is well known as Cauchy's theorem or Cauchy's surface area formula, [57, 58].

The formula states that the surface area of a convex body $S_{p,c}$ is four times the projection area averaged over several projections $\overline{A_{p,c}}$.

$$S_{p,c} = 4\overline{A_{p,c}} \tag{20}$$

This theorem can be tested directly on the simulated data, not so much to prove the theorem, but to test the validity of the dataset. Fig. 15 shows the relations of surface area and projection area, both for the actual particles and their convex hulls. Note that single points are plotted, not actual averaged values, so Cauchy's theorem may only hold on the average, which is why linear regression lines are included. For the soda-lime glass convex hulls (Fig. 15b), the value of 3.98 is particularly close to the theoretical value, while for the compact particles it is only slightly smaller at 3.90. For mica particles, the values significantly decrease. The lower regression value for mica is expected, as it is very likely for a flaky particle to produce silhouettes of comparably lower projection area.

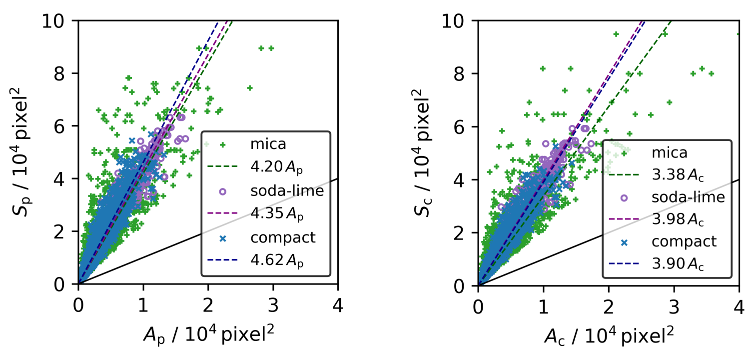

(a) Particle surface area vs. projection area

(b) Convex surface area vs. convex projection area

Figure 15: Correlations of surface area and projection area for *random orientations*

For the relation of actual particle surface and projection area, i.e., of the non-convex shapes, surface area is underestimated for all particles: when Cauchy's theorem would be used, surface area would be predicted to be smaller than the actual value(s). This trend is caused by the rugged surface that cannot be properly estimated by projections, as most concavities will be hidden in the projection image – an effect that can be much larger for very rough particles [29].

4.2. Particle Width–Feret Correlation

As mentioned in the introduction, dynamic image analysis is widely used to replace sieve analysis. More often than not, data from a dynamic image analysis system needs to be adjusted to account for divergence of the measurements from a sieve analysis. When sieving is done on square aperture sieve meshes, particles will be classified according to their intermediate dimension, width w. In static image analysis, particle width is very well determined by the minimum Ferets, $x_{\mathrm{Fe,min}}$ or $x_{\mathrm{Fe,min90}}$ (cf. Fig 14). However, in dynamic image analysis it is only possible to know the three main particle dimensions l, w, and t by imaging single particles from different angles or by tracking rotating particles while they fall through the measurement system [26, 60].

Using the dataset of random orientations, aspect ratio AR was found to be the underlying variable explaining the deviation of both the minimum $x_{\mathrm{Fe,min}}$ and maximum Feret diameters $x_{\mathrm{Fe,max}}$ from particle width w. The following correlation was found to predict particle width very well:

$$w \approx x_{\mathrm{Fe,max}} \sqrt{\mathrm{AR}} \tag{21}$$

Furthermore, because of the definition of aspect ratio, Eq. 6:

$$w \approx x_{\mathrm{Fe,max}} \sqrt{\mathrm{AR}} = \frac{x_{\mathrm{Fe,min}}}{\sqrt{\mathrm{AR}}} = \sqrt{x_{\mathrm{Fe,max}}\, x_{\mathrm{Fe,min}}} \tag{22}$$

The correlation defined by Eq. 21 is shown in Fig. 16a. For the compact particles, the agreement between 2D and 3D parameters is quite excellent. Even for the non-compact mica particles, the correlation holds, though the scatter is expectedly larger. Fig. 16b gives the relative deviation of width estimates from actual particle width. For compact particles, the 95 % CI is within a deviation of ±25 %, while the mean is within a ±5 % interval.

The relevant particle dimension for sieve analysis, width w, is therefore expected to be approximated well with any of the expressions of Eq. 22.

4.3. Sphericity Correlation

Circularity ψ_{c} (Eq. 12) is often used in place of sphericity ψ_{Wa} (Eq. 8) because the former is much easier to measure in static or dynamic imaging setups [59]. It was therefore deemed a worthwhile exercise to see how well circularity and sphericity correlate for the dynamic imaging simulation.

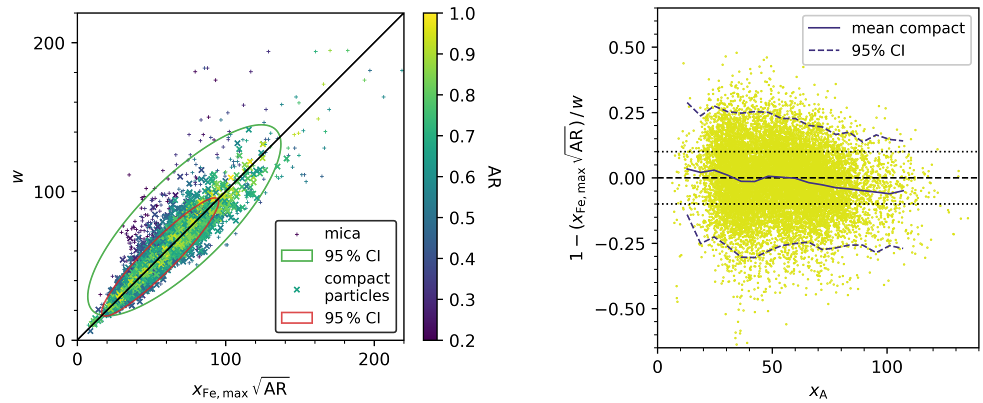

(a) 95 % confidence ellipses

(b) Relative error over area–equivalent diameter *for compact particles*

Figure 16: Correlation of Feret diameters with particle width w

4.3.1. *Mica*

Fig. 17 shows plots of Wadell's sphericity ψ_{Wa} over circularity ψ_{c}. The first insight is in regards to extremely small correlation values of the shape factors in the correlation matrices (Fig. 13b): at first sight, there is only a point cloud with no tendency whatsoever.

At second sight, because of the nature of the two shape factors, both should be zero for infinitely stretched objects and one for spheres. Because of this unique relationship, a linear regression needs no offset, i.e., should start from zero. If a linear regression then returns a slope of one, the two shape factors are perfectly correlated. Any spread in either direction is then purely stochastic. The term "stochastic" here signifies the inherent scatter of imaging particles at random orientations, not measurement error.

From Fig. 17a it can be seen that the correlation between circularity ψ_{c} and sphericity ψ_{Wa} is rather non-ideal, whereas the square root of sphericity $\sqrt{\psi_{\mathrm{Wa}}}$ leads a much better linear regression slope of 1.06.

Another way to evaluate the two parameter pairs is to plot the 95 % confidence interval (CI). Because the data is two-dimensional, confidence ellipses are calculated, as shown in Fig. 17b, that include 95 % of particles under the assumption that the point cloud is normally distributed for both variables. As shown, the center of the ellipse of $\sqrt{\psi_{\mathrm{Wa}}}$ vs. ψ_{c} (in green) is much closer to the equality line then the ellipse for ψ_{Wa} vs. ψ_{c} (in blue).

Squaring the new-found relationship gives sphericity ψ_{Wa} over the form

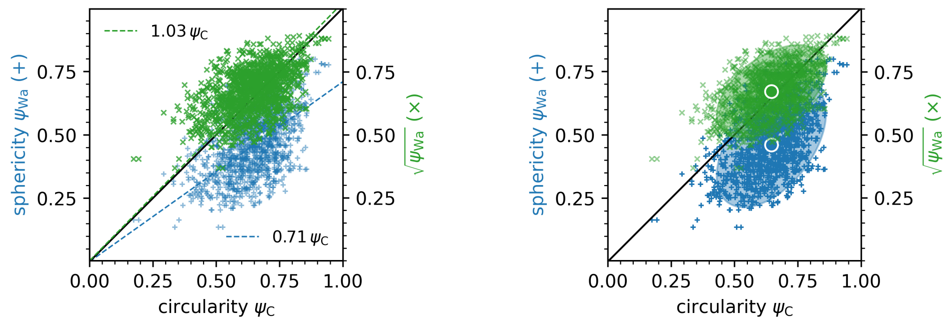

(a) Linear regression results (b) 95 % confidence ellipses

Figure 17: Correlation of sphericity and its square root with circularity *for mica particles* at *random orientations*

factor $\mathrm{FF} = \psi_{\mathrm{c}}^2$:

$$\psi_{\mathrm{Wa}} \approx \mathrm{FF} \tag{23}$$

Estimates of the shape factors are summarized for all solids in Table 2. Interestingly, the correlation works very well for the flaky mica, whereas it doesn't fit nearly as well for the other solids.

4.3.2. Compact Particles

Starting from the relationship found for mica, Eq. 23, variables where evaluated that could explain the deviation of the compact particles from true equality. The best relationship, which is an extension of Eq. 23, is:

$$\psi_{\mathrm{Wa}} \approx \mathrm{FF}\,\sqrt{\psi_{\mathrm{c,bc}}}\;/\;C_{\mathrm{x,2D}}^2 \tag{24}$$

The linear regression results and confidence ellipses for Eq. 24 are shown in Figs. 18a and 18c. Except for the highly spherical soda-lime glass, the relationship seems to slightly overestimate Wadell's sphericity. Additionally, Fig. 18e shows the relative error of Eq. 24's estimates for sphericity as a rolling mean over projection area–equivalent particle diameter x_{A} and the corresponding 95 % CI. The relative error for the compact particles is again showing a slight overestimation of sphericity for particle sizes, hinting at a yet to be found explanatory variable. However, the error for the mean is below 10 % for all particle sizes.

A downside in the usability of Eq. 24 for prediction of Wadell's sphericity is that both the form factor FF (Eq. 13) and convexity $C_{\mathrm{x,2D}}$ (Eq. 19) depend on accurate determination of the projection perimeter P_{p}, which

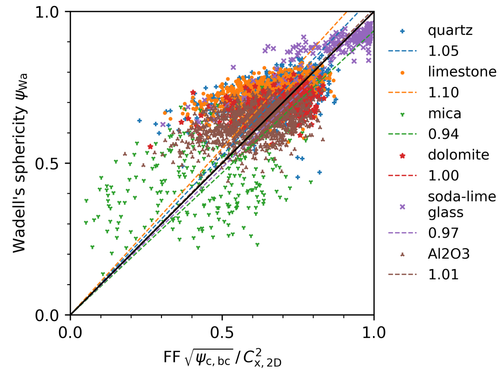

(a) Linear regression results for Eq. 24

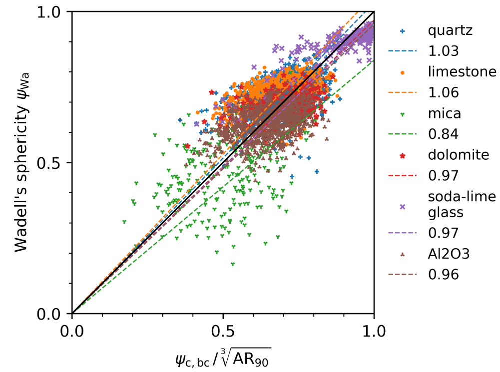

(b) Linear regression results for Eq. 25

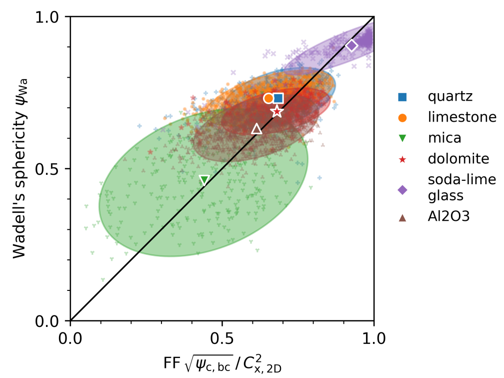

(c) 95 % CI ellipses for Eq. 24

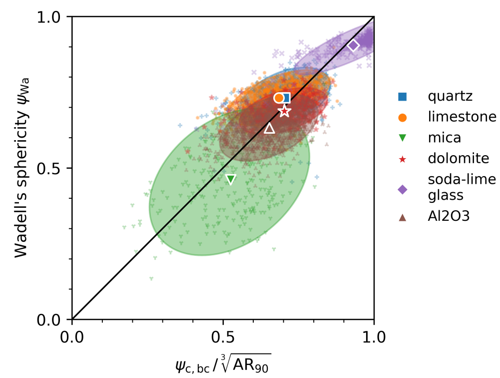

(d) 95 % CI ellipses for Eq. 25

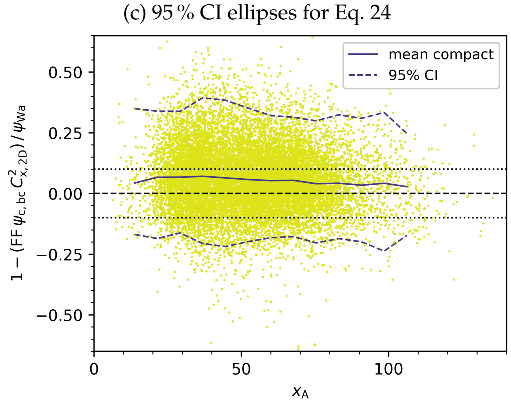

(e) Relative error *for compact particles* over (projection) area–equivalent diameter for Eq. 24

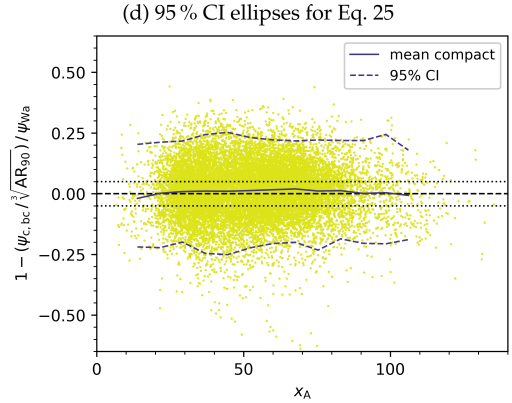

(f) Relative error *for compact particles* over (projection) area–equivalent diameter for Eq. 25

Figure 18: Correlation of 2D shape factors and Wadell's sphericity for the dynamic image analysis case (*random orientations*)

will lead to resolution problems for small particles, as demonstrated by the increased error for smaller particle sizes in Fig. 18e.

Therefore another correlation was developed which does not depend on the accurate determination of perimeter. Instead, it only uses aspect ration and bounding circles' circularity:

$$\psi_{\mathrm{Wa}} \approx \psi_{\mathrm{c,bc}} \,/\, \sqrt[3]{\mathrm{AR}_{90}} \tag{25}$$

While this second correlation is simpler, it also leads to an improved prediction of Wadell's sphericity, as shown in Figs. 18b, 18d, and 18f. The relative error for the mean stays below 2 %. The correlation may even be useful for estimation of single particle sphericity values, because the 95 % CI stays within a range of ±25 %.

Average sphericity predictions are summarized in Table 2. Eq. 25 is clearly superior compared to Eq. 24. Only in the case of mica, Eq. 24 provides a better average estimate of sphericity, which may hint at the correlation being more accurate in the case of plate-like particles. However, for mica even the form factor is a fairly accurate predictor of sphericity.

Table 2: Average sphericities ψ_{Wa} determined with the correlation equations 23, 24, and 25; intervals shown are the standard deviations from the mean

		equation		
		23	24	25
material	ψ_{Wa} (3D)	FF	FF $\sqrt{\psi_{\mathrm{c,bc}}} \,/\, C^2_{\mathrm{x,2D}}2$	$\psi_{\mathrm{c,bc}} \,/\, \sqrt[3]{\mathrm{AR}_{90}}$
quartz	0.73 ± 0.05	0.63 ± 0.16	0.69 ± 0.09	0.71 ± 0.08
limestone	0.73 ± 0.05	0.58 ± 0.16	0.65 ± 0.11	0.69 ± 0.08
mica	0.46 ± 0.12	0.43 ± 0.13	0.44 ± 0.17	0.52 ± 0.13
dolomite	0.69 ± 0.04	0.59 ± 0.12	0.68 ± 0.09	0.70 ± 0.07
soda-lime	0.91 ± 0.05	0.78 ± 0.18	0.93 ± 0.11	0.93 ± 0.09
Al_2O_3	0.63 ± 0.05	0.54 ± 0.13	0.61 ± 0.10	0.65 ± 0.08

Note that the predictive value is reasonably good because of the large number of data points. If there had been only a handful of particles, the final correlation would have been nearly impossible to find. Furthermore, the predictive power may not hold for all types of solids.

Especially for Eq. 24, because of the use of convexity, effects of image resolution could come into play which have not been part of this study, but are planned to be investigated in the future. If surface roughness significantly increases, surface area effects could be underestimated by 2D convexity [29], because the fractal behavior of surface roughness cannot be accurately determined by 2D imaging techniques. Because the resolution of STL mesh, voxel image, and projection silhouette are directly linked in this study, the correlation is expected to give sphericity values *for the resolution* of the image acquisition.

Consider the following example. At a pixel dimension of 2 µm, Eq. 24 will give a sphericity value that is valid at the same (3D) voxel resolution of 2 µm. If a highly rugged 3D particle surface is measured at a higher resolution, i.e., $\ll 2$ µm in the example, particle surface will increase and Wadell's sphericity value decrease. Of course, this resolution effect is mostly mitigated by use of Eq. 25, which does not rely on projection perimeter at all.

How could Eq. 25 be used in practice? It needs to be understood that this correlation is not able to predict sphericities of single particles accurately, which is apparent from the scatter in Fig. 18a. However, what the correlation can achieve is the prediction of a mean sphericity for a given bulk solids, which is in most cases the only needed information. Of course, as demonstrated by Fig. 18f, size-dependent sphericity determination is possible in principle.

5. Validation Measurements

Dynamic image analysis measurements were performed to validate the correlations found in sections 4.3 and 4.2. For the experiments, the Fritsch Analysette 28 ImageSizer was used. An example image is shown in Fig. 19a. The acquired images were evaluated externally with a Python script, because the machine's software doesn't calculate all the necessary 2D shape factors, in particular the bounding circle diameters. Only particles with very sharp contours were extracted and particles that were not clearly isolated or touched the image boundaries were discarded. Fig. 19b shows particles isolated from the example image. Distributions of minimum Feret diameters and circularities as given by the ImageSizer analysis software were found to be in excellent agreement with the distributions found by the Python script.

All six solids used in this text were measured with the dynamic image analysis system. However, only the compact particles were evaluated,

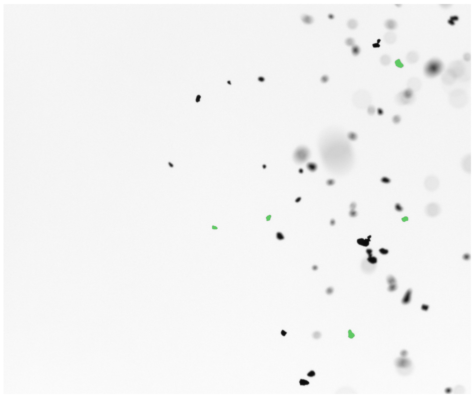

(a) Example image with extracted particles highlighted in green

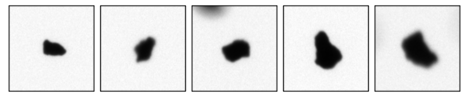

(b) Extracted (sharp) particles

Figure 19: Example image of dynamic image measurement of limestone

because the mica particles reflected light extremely well, which led to problems in image evaluation. Images are still available in a supplementary dataset, see below.

Fig. 20a shows the distribution of minimum Feret diameters $x_{\mathrm{Fe,min}}$ extracted from the dynamic image measurements in comparison to the 3D particle widths for limestone particles. The discrepancy between the two distributions is noticeably decreased by use of Eq. 22. Not only is the average particle width estimated well, the overall distribution is predicted well, with percentiles shown in Table 3; as expected, the predicted values are a little further spread apart, with additional spread originating in the random particle orientations that themselves produce an element of dispersion.

Table 3: Quantiles for particle width estimators

percentile	w	$x_{\mathrm{Fe,min}}$	$x_{\mathrm{Fe,min}}\sqrt{\mathrm{AR}}$
10	65.0	50.9	62.6
20	71.7	57.7	70.4
50	95.3	75.9	94.9
80	131.4	114.7	138.1
90	153.2	138.0	168.8

Using log-spaced size classes for the actual and estimated particle

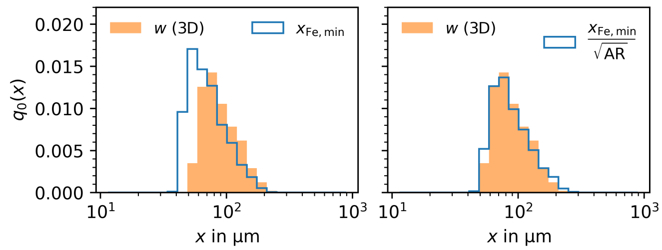

(a) Probability densities for limestone particles: 2D minimum Feret diameter $x_{\mathrm{Fe,min}}$ and estimated particle width $x_{\mathrm{Fe,min}}/\sqrt{\mathrm{AR}}$ according to section 4.2 in comparison to actual 3D particle width w

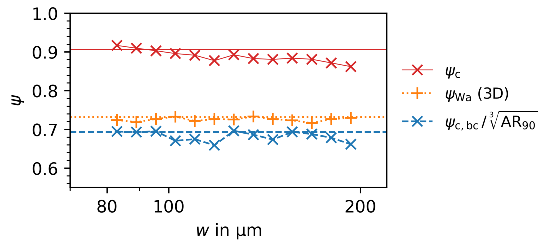

(b) Estimated sphericities (Eq. 25) as function of particle width for limestone particles

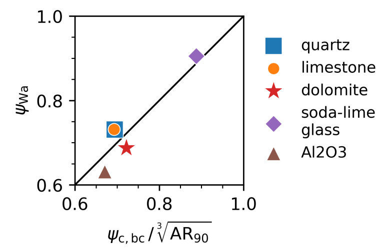

(c) Estimated sphericities for the investigated compact solids

Figure 20: Validation of the correlations found in the text with dynamic image analysis measurements

widths, particle sphericity ψ_{Wa} is estimated with Eq. 25, the result of which is shown in Fig. 20b. As shown, the actual sphericity per the 3D particle data is slightly underestimated. However, the estimate is much more usable than using circularity ψ_{c}. In fact, Eq. 25 is very much usable for all the investigated solids, with Fig. 20c showing the average sphericity values in 3D against the 2D estimates.

In theory, the correlations validated here could have been found through separate, i.e., stand-alone, 3D and 2D measurements. However, the simulated dataset gives the direct relation between 2D and 3D particle characteristics for *every single* particle, which makes the analysis much more robust. Note that the use of the dataset is not limited to the findings of this text, but is expected to hold many more insights into the relationships between 2D and 3D particle measurements.

6. Conclusions

A collection of particle surface meshes, resulting from X-ray tomographic measurements, has been used to simulate both static and dynamic image analysis. The results have been evaluated to find the highest correlations between 2D and 3D geometric measures and shape factors. The dataset and methods described prove to be physically accurate and are tested against validation measurements.

Examples have been given of the potential insights this dataset may generate. Predictive correlations for Wadell's sphericity in 3D have been found that are expected to predict sphericity values well for a wide range of particles using only 2D shape descriptors, provided that enough particles are measured. The most suitable correlation was found to be Eq. 24:

$$\psi_{\mathrm{Wa}} \approx \psi_{\mathrm{c,bc}} \,/\, \sqrt[3]{\mathrm{AR}_{90}}$$

In the same vein, a correlation for estimating particle width from 2D Feret diameters has been determined, Eq. 21:

$$w \approx x_{\mathrm{Fe,max}} \sqrt{\mathrm{AR}} = x_{\mathrm{Fe,min}} \,/\, \sqrt{\mathrm{AR}} = \sqrt{x_{\mathrm{Fe,max}}\, x_{\mathrm{Fe,min}}}$$

Confirmation experiments with a broader set of particles are planned in the future. An inherent measurement artifact of image analysis, pixel resolution, needs to be investigated, but is expected to be negligible for a large enough number of pixels as proven by validation experiments (**??**).

The dataset, as provided in the supplementary data, offers the possibility to discover numerous correlations and insights regarding geometric measures and shape factors, as well as their relationships across two and three dimensions. We encourage researchers to use the dataset for their research questions and to shed light into questions that had long been obscured by computational complexity.

Supplementary Data

Supplementary files are available in the Open Access Repository and Archive for Research Data of Saxon Universities (OPARA):

`https://doi.org/10.25532/OPARA-479`
`https://doi.org/10.25532/OPARA-587`
`https://doi.org/10.25532/OPARA-595`

The supplementary files enable users to reproduce imaging datasets as used in this study and demonstrate the methods for acquisition of all particle characteristics for an example particle. Particle STL files are included in the first entry above. The second entry extends the code by determination of surface area via `MorphoLibJ` and a dynamic imaging dataset of ten random orientations per particle instead of the previous three. The final entry includes results from dynamic image analysis measurements for validation. Note that you need a working Python setup and that all code is made available as Jupyter notebooks.

Acknowledgements

We would like to express our gratitude to the Institute of Foundry Technology at TU Bergakademie Freiberg for letting us use their Analysette 28 ImageSizer for image analysis measurements.

This research work was supported by the German Federal Ministry of Education and Research through the research project InfraDatRec (grant no. 03XP0426A).

Appendix A. Wadell's Circularity

One correlation found, that is not necessarily expected, is between Wadell's alternative circularity definition $\psi_{\mathrm{c,Wa}}$ (Eq. 14) and the bounding circles circularity $\psi_{\mathrm{c,bc}}$ (Eq. 15). Though it is a correlation between two 2D shape factors, it is too interesting to ignore. As predicted by the correlation matrix in Fig. 11a, where the correlation is found in the lower right (second) quadrant between values 46 ($\psi_{\mathrm{c,Wa}}$) and 47 ($\psi_{\mathrm{c,bc}}$), there is a near-perfect linear relationship. However, to have the two circularities directly coincide, Wadell's circularity is squared, $\psi^2_{\mathrm{c,Wa}}$. The resulting correlation is shown in Fig. A.21a.

Because of the definitions of the two circularities, it is found that the area–equivalent diameter is directly related to the bounding circle diameters.

$$x_{\mathrm{A}}^2 \approx d_{\mathrm{ic}}\, d_{\mathrm{ec}} \tag{A.1}$$

The above relationship is shown in Fig. A.21b.

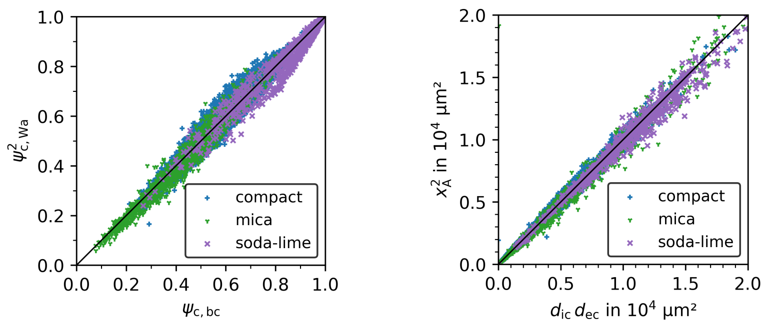

(a) Wadell's circularity vs. bounding circles circularity

(b) Area-equivalent diameter vs. bounding circles diameters

Figure A.21: Correlation of Wadell's alternative definition for circularity (Eq. 14) and bounding circles circularity (Eq. 15)

Appendix B. Particle characteristics

Table B.1 gives a list of the particle characteristics as used in the correlation matrices, Figs. 11 and 13.

References

[1] T. Buchwald, E. Schach, U. A. Peuker, A framework for the description of multidimensional particle separation processes, Powder Technology 433 (2024) 119165. doi:10.1016/j.powtec.2023.119165.

[2] E. Schach, T. Buchwald, T. Leißner, U. Peuker, R. T. Delgado, Concepts of entropy for raw materials, Powder Technology 435 (2024) 119398. doi:10.1016/j.powtec.2024.119398.

[3] U. Ulusoy, C. Igathinathane, Particle size distribution modeling of milled coals by dynamic image analysis and mechanical sieving, Fuel Processing Technology 143 (2016) 100–109. doi:10.1016/j.fuproc.2015.11.007.

[4] J. Fernlund, 3-d image analysis size and shape method applied to the evaluation of the los angeles test, Engineering Geology 77 (2005) 57–67. doi:10.1016/j.enggeo.2004.08.002.

[5] S. Durand, B. E. Jackson, W. C. Fonteno, J. Michel, Particle size distribution of growing media constituents using dynamic image analysis:

Table B.1: Particle characteristics

no.		category	name	symbol	dimensions	equation
			3D characteristics			
1		I	particle volume	V_{p}	L^3	–
2			convex volume	V_{c}	L^3	–
3			volume-equivalent diameter	x_{V}	L^1	2
4			convex volume-eq. diameter	$x_{\mathrm{V,c}}$	L^1	–
5		II	particle surface area	S_{p}	L^2	–
6			convex surface area	S_{c}	L^2	–
7			surface-equivalent diameter	x_{S}	L^1	3
8			convex surface-eq. diameter	$x_{\mathrm{S,c}}$	L^1	–
9			volume-specific surface area	S_{V}	L^{-1}	–
10		III	aligned length	l	L^1	–
11			oriented length	l_{oriented}	L^1	–
12		IV	aligned width	w	L^1	–
13			oriented width	w_{oriented}	L^1	–
14		V	aligned thickness	t	L^1	–
15			oriented thickness	t_{oriented}	L^1	–
16		VI	min. enclosing sphere diameter	d_{es}	L^1	–
17			max. inscribed sphere diameter	d_{is}	L^1	–
18		VII	elongation	w/l	–	–
19			flatness	t/w	–	–
20		VIII	Wadell's sphericity	ψ_{Wa}	–	8
21			Krumbein's sphericity	ψ_{Kr}	–	9
22			bounding spheres sphericity	ψ_{Wa}	–	10
23			Hofmann's sphericity	ψ_{Ho}	–	11
24		IX	3D solidity	$S_{\mathrm{x,3D}}$	–	16
25			3D convexity	$C_{\mathrm{x,3D}}$	–	18
			2D characteristics			
26	1	I	projection area	A_{p}	L^2	–
27	2		convex projection area	A_{c}	L^2	–
28	3		area-equivalent diameter	x_{A}	L^1	4
29	4		convex area-eq. diameter	$x_{\mathrm{A,c}}$	L^1	–
30	5	II	projection perimeter	P_{p}	L^1	–
31	6		convex projection perimeter	P_{c}	L^1	–
32	7		perimeter-equivalent diameter	x_{P}	L^1	5
33	8		convex perimeter-eq. diameter	$x_{\mathrm{P,c}}$	L^1	–
34	9	III	bounding box length	l_{bb}	L^1	–
35	10		maximum Feret diameter	$x_{\mathrm{Fe,max}}$	L^1	–
36	11		orthogonal Feret to $x_{\mathrm{Fe,min}}$	$x_{\mathrm{Fe,max90}}$	L^1	–
37	12	IV	bounding box width	w_{bb}	L^1	–
38	13		minimum Feret diameter	$x_{\mathrm{Fe,min}}$	L^1	–
39	14		orthogonal Feret to $x_{\mathrm{Fe,max}}$	$x_{\mathrm{Fe,min90}}$	L^1	–
40	15	V	min. enclosing circle diameter	d_{ec}	L^1	–
41	16		max. inscribed circle diameter	d_{ic}	L^1	–
42	17	VI	aspect ratio	AR	–	–
43	18		orthogonal aspect ratio	AR_{90}	–	–
44	19	VII	circularity	ψ_{c}	–	12
45	20		form factor	FF	–	13
46	21		Wadell's circularity	$\psi_{\mathrm{c,Wa}}$	–	14
47	22		bounding circles circularity	$\psi_{\mathrm{c,bc}}$	–	15
48	23	VIII	2D solidity	$S_{\mathrm{x,2D}}$	–	17
49	24		2D convexity	$C_{\mathrm{x,2D}}$	–	19

Parametrization and comparison to sieving, Soil Science Society of America Journal 87 (2023) 767–780. doi:10.1002/saj2.20518.

[6] J. Emmerich, Q. Tang, Y. Wang, P. Neubauer, S. Junne, S. Maaß, Optical inline analysis and monitoring of particle size and shape distributions for multiple applications: Scientific and industrial relevance, Chinese Journal of Chemical Engineering 27 (2019) 257–277. doi:10.1016/j.cjche.2018.11.011.

[7] D. M. Scott, Recent advances in in-process characterization of suspensions and slurries, Powder Technology 399 (2022) 117159. doi:10.1016/j.powtec.2022.117159.

[8] H. Wadell, Volume, shape, and roundness of rock particles., The Journal of Geology 40 (1932) 443–451.

[9] H. Wadell, Sphericity and roundness of rock particles, The Journal of Geology 41 (1933) 310–331. doi:10.1086/624040.

[10] B. C. Aschenbrenner, A new method of expressing particle sphericity, SEPM Journal of Sedimentary Research 26 (1956). doi:10.1306/74d704a7-2b21-11d7-8648000102c1865d.

[11] Zingg, Theodor, Beitrag zur Schotteranalyse, Ph.D. thesis, ETH Zürich, 1935. doi:10.3929/ETHZ-A-000103455.

[12] V. Angelidakis, S. Nadimi, S. Utili, Shape analyser for particle engineering (shape): Seamless characterisation and simplification of particle morphology from imaging data, Computer Physics Communications 265 (2021) 107983. doi:10.1016/j.cpc.2021.107983.

[13] T. Yao, W. Li, Quantifying the particle shape and surface roughness of sands, Bulletin of Engineering Geology and the Environment 82 (2023). doi:10.1007/s10064-023-03167-7.

[14] D. Su, W. M. Yan, Prediction of 3d size and shape descriptors of irregular granular particles from projected 2d images, Acta Geotechnica 15 (2019) 1533–1555. doi:10.1007/s11440-019-00845-3.

[15] X. Wang, K. Tian, D. Su, J. Zhao, Superellipsoid-based study on reproducing 3d particle geometry from 2d projections, Computers

and Geotechnics 114 (2019) 103131. doi:10.1016/j.compgeo.2019.103131.

[16] W.-Q. Xie, X.-P. Zhang, X.-M. Yang, Q.-S. Liu, S.-H. Tang, X.-B. Tu, 3d size and shape characterization of natural sand particles using 2d image analysis, Engineering Geology 279 (2020) 105915. doi:10.1016/j.enggeo.2020.105915.

[17] C. H. Lee, S. J. Lee, M. Shin, Characterization of variability in 2-dimensional particle geometry via 3d structured light scanning, Transportation Geotechnics 34 (2022) 100760. doi:10.1016/j.trgeo.2022.100760.

[18] X. Jia, R. Liu, H. Ren, Y. Han, J. Ouyang, H. Zheng, C. Peng, J. Zheng, Particle shape characterizations for energetic materials by computational geometry and stereology method, SN Applied Sciences 4 (2022). doi:10.1007/s42452-022-05031-x.

[19] R. D. Beemer, L. Li, A. Leonti, J. Shaw, J. Fonseca, I. Valova, M. Iskander, C. H. Pilskaln, Comparison of 2d optical imaging and 3d microtomography shape measurements of a coastal bioclastic calcareous sand, Journal of Imaging 8 (2022) 72. doi:10.3390/jimaging8030072.

[20] G. Bagheri, C. Bonadonna, I. Manzella, P. Vonlanthen, On the characterization of size and shape of irregular particles, Powder Technology 270 (2015) 141–153. doi:10.1016/j.powtec.2014.10.015.

[21] G. Mollon, J. Zhao, 3d generation of realistic granular samples based on random fields theory and fourier shape descriptors, Computer Methods in Applied Mechanics and Engineering 279 (2014) 46–65. doi:10.1016/j.cma.2014.06.022.

[22] T. Ueda, Estimation of three-dimensional particle size and shape characteristics using a modified 2d–3d conversion method employing spherical harmonic-based principal component analysis, Powder Technology 404 (2022) 117461. doi:10.1016/j.powtec.2022.117461.

[23] P. Zhang, Z. Yin, Y. Jin, Three-dimensional quantitative analysis on granular particle shape using convolutional neural network, International Journal for Numerical and Analytical Methods in Geomechanics 46 (2021) 187–204. doi:10.1002/nag.3296.

[24] K. Giannis, C. Thon, G. Yang, A. Kwade, C. Schilde, Predicting 3d particles shapes based on 2d images by using convolutional neural network, Powder Technology 432 (2024) 119122. doi:10.1016/j.powtec.2023.119122.

[25] C. Rao, E. Tutumluer, J. Stefanski, Coarse aggregate shape and size properties using a new image analyzer, Journal of Testing and Evaluation 29 (2001) 461–471. doi:10.1520/jte12276j.

[26] A. K. Rajagopalan, J. Schneeberger, F. Salvatori, S. Bötschi, D. R. Ochsenbein, M. R. Oswald, M. Pollefeys, M. Mazzotti, A comprehensive shape analysis pipeline for stereoscopic measurements of particulate populations in suspension, Powder Technology 321 (2017) 479–493. doi:10.1016/j.powtec.2017.08.044.

[27] R. Ditscherlein, O. Furat, E. Löwer, R. Mehnert, R. Trunk, T. Leißner, M. J. Krause, V. Schmidt, U. A. Peuker, Parrot: A pilot study on the open access provision of particle-discrete tomographic datasets, Microscopy and Microanalysis 28 (2022) 350–360. doi:10.1017/s143192762101391x.

[28] T. S. Newman, H. Yi, A survey of the marching cubes algorithm, Computers & Graphics 30 (2006) 854–879. doi:10.1016/j.cag.2006.07.021.

[29] T. Buchwald, G. Schmandra, L. Schützenmeister, T. Fraszczak, T. Mütze, U. Peuker, Gaseous flow through coarse granular beds: The role of specific surface area, Powder Technology 366 (2020) 821–831. doi:10.1016/j.powtec.2020.03.028.

[30] G. Bradski, The OpenCV Library, Dr. Dobb's Journal of Software Tools (2000).

[31] P. Virtanen, R. Gommers, T. E. Oliphant, M. Haberland, T. Reddy, D. Cournapeau, E. Burovski, P. Peterson, W. Weckesser, J. Bright, S. J. van der Walt, M. Brett, J. Wilson, K. J. Millman, N. Mayorov, A. R. J. Nelson, E. Jones, R. Kern, E. Larson, C. J. Carey, İ. Polat, Y. Feng, E. W. Moore, J. VanderPlas, D. Laxalde, J. Perktold, R. Cimrman, I. Henriksen, E. A. Quintero, C. R. Harris, A. M. Archibald, A. H. Ribeiro,

F. Pedregosa, P. van Mulbregt, SciPy 1.0 Contributors, SciPy 1.0: Fundamental Algorithms for Scientific Computing in Python, Nature Methods 17 (2020) 261–272. doi:10.1038/s41592-019-0686-2.

[32] B. Zhao, J. Wang, 3d quantitative shape analysis on form, roundness, and compactness with μct, Powder Technology 291 (2016) 262–275. doi:10.1016/j.powtec.2015.12.029.

[33] J. Zheng, R. D. Hryciw, Traditional soil particle sphericity, roundness and surface roughness by computational geometry, Géotechnique 65 (2015) 494–506. doi:10.1680/geot.14.p.192.

[34] W. E. Lorensen, H. E. Cline, Marching cubes: A high resolution 3d surface construction algorithm, in: Proceedings of the 14th annual conference on Computer graphics and interactive techniques, SIGGRAPH '87, ACM, 1987, pp. 163–169. doi:10.1145/37401.37422.

[35] T. Lewiner, H. Lopes, A. W. Vieira, G. Tavares, Efficient implementation of marching cubes' cases with topological guarantees, Journal of Graphics Tools 8 (2003) 1–15. doi:10.1080/10867651.2003.10487582.

[36] J. Lindblad, I. Nyström, Surface Area Estimation of Digitized 3D Objects Using Local Computations, Springer Berlin Heidelberg, 2002, pp. 267–278. doi:10.1007/3-540-45986-3_24.

[37] D. Legland, I. Arganda-Carreras, P. Andrey, Morpholibj: integrated library and plugins for mathematical morphology with imagej, Bioinformatics 32 (2016) 3532–3534. doi:10.1093/bioinformatics/btw413.

[38] G. Lehmann, D. Legland, Efficient n-dimensional surface estimation using crofton formula and run-length encoding, The Insight Journal (2012). doi:10.54294/wdu86d.

[39] C. Lang, J. Ohser, R. Hilfer, On the analysis of spatial binary images, Journal of Microscopy 203 (2001) 303–313. doi:10.1046/j.1365-2818.2001.00899.x.

[40] W. C. Krumbein, Measurement and geological significance of shape and roundness of sedimentary particles, SEPM Journal of Sedimentary Research Vol. 11 (1941). doi:10.1306/d42690f3-2b26-11d7-8648000102c1865d.

[41] E. D. Sneed, R. L. Folk, Pebbles in the lower colorado river, texas a study in particle morphogenesis, The Journal of Geology 66 (1958) 114–150. URL: http://www.jstor.org/stable/30058239. doi:10.2307/30058239.

[42] J. W. Bullard, E. J. Garboczi, Defining shape measures for 3d star-shaped particles: Sphericity, roundness, and dimensions, Powder Technology 249 (2013) 241–252. doi:10.1016/j.powtec.2013.08.015.

[43] H. J. Hofmann, Grain-shaped indices and isometric graphs, Journal of Sedimentary Research 64 (1994) 916–920. doi:10.1306/d4267f0a-2b26-11d7-8648000102c1865d.

[44] J. P. Le Roux, Comparison of sphericity indices as related to the hydraulic equivalence of settling grains, SEPM Journal of Sedimentary Research Vol. 67 (1997). doi:10.1306/d42685bd-2b26-11d7-8648000102c1865d.

[45] N. A. Riley, Projection sphericity, SEPM Journal of Sedimentary Research Vol. 11 (1941). doi:10.1306/d426910c-2b26-11d7-8648000102c1865d.

[46] E. P. Cox, A method of assigning numerical and percentage values to the degree of roundness of sand grains, Journal of Paleontology 1 (1927) 179–183. URL: http://www.jstor.org/stable/1298056. doi:10.2307/1298056.

[47] N. Ritter, J. Cooper, New resolution independent measures of circularity, Journal of Mathematical Imaging and Vision 35 (2009) 117–127. doi:10.1007/s10851-009-0158-x.

[48] M. Pons, H. Vivier, K. Belaroui, B. Bernard-Michel, F. Cordier, D. Oulhana, J. Dodds, Particle morphology: from visualisation to measurement, Powder Technology 103 (1999) 44–57. doi:10.1016/s0032-5910(99)00023-6.

[49] R. Ditscherlein, T. Leißner, U. A. Peuker, Preparation techniques for micron-sized particulate samples in x-ray microtomography, Powder Technology 360 (2020) 989–997. doi:10.1016/j.powtec.2019.06.001.

[50] R. Ditscherlein, T. Leißner, U. A. Peuker, Self-constructed automated syringe for preparation of micron-sized particulate samples in x-ray microtomography, MethodsX 7 (2020) 100757. doi:10.1016/j.mex.2019.11.030.

[51] V. C. Janoo, Quantification of Shape, Angularity, and Surface texture of Base Course Materials, Special report 98-1, Cold Regions Research and Engineering Laboratory (U.S.), 1998. URL: https://rosap.ntl.bts.gov/view/dot/14065.

[52] V. Angelidakis, S. Nadimi, S. Utili, Elongation, flatness and compactness indices to characterise particle form, Powder Technology 396 (2022) 689–695. doi:10.1016/j.powtec.2021.11.027.

[53] International Organization for Standardization, Particle size analysis—image analysis methods—part 1: Static image analysis methods (ISO 13322-1:2014), Standard, 2014.

[54] Dawson-Haggerty et al., trimesh, 2024. URL: https://trimesh.org/.

[55] S. Gillies, C. van der Wel, J. Van den Bossche, M. W. Taves, J. Arnott, B. C. Ward, et al., Shapely, 2024. doi:10.5281/ZENODO.5597138.

[56] International Organization for Standardization, Particle size analysis—image analysis methods—part 2: Dynamic image analysis methods (ISO 13322-2:2021), Standard, 2021.

[57] V. Vouk, Projected area of convex bodies, Nature 162 (1948) 330–331. doi:10.1038/162330a0.

[58] B. Meltzer, Shadow area of convex bodies, Nature 163 (1949) 220–220. doi:10.1038/163220b0.

[59] J. R. Grace, A. Ebneyamini, Connecting particle sphericity and circularity, Particuology 54 (2021) 1–4. doi:10.1016/j.partic.2020.09.006.

[60] L. Li, M. Iskander, Comparison of 2d and 3d dynamic image analysis for characterization of natural sands, Engineering Geology 290 (2021) 106052. doi:10.1016/j.enggeo.2021.106052.